China Geology 8 (2025) 159−186

China Geology

Journal homepage: http://chinageology.cgs.cn
https://www.sciencedirect.com/journal/china-geology

Geochemistry and petrogenesis of Mesoproterozoic mafic granulite and amphibolite dykes from Saltora, Bankura district, Chhotanagpur Gneissic Complex, eastern India: Implications for their emplacement in within-plate setting

Poulami Roy, Bapi Goswami*, Ankita Basak, Anwesa Sen, Chittaranjan Bhattacharyya

Department of Geology, University of Calcutta, 35 Ballygunge Circular Road, Kolkata 700019, *India*

ARTICLE INFO

Article history:
Received 1 September 2022
Received in revised form 2 May 2023
Accepted 16 May 2023
Available online 25 May 2023

Keywords:
Metamorphosed mafic dykes
Within-plate basaltic magmatism
Carbonated spinel-peridotite
Chhotanapgpur Gneissic Complex
Mesoproterozoic
Continental rift
Crustal extension
SCLM
Petrogenesis
India

ABSTRACT

Distinguishing high-grade mafic-ultramafic rocks originally crystallized from within-plate basaltic magmatism is challenging and crucial because the chemical composition of the igneous rocks has been modified during high-grade metamorphism, causing misidentification of the characters of the parental magma. Proterozoic metamorphosed mafic dykes occur throughout the Chhotanagpur Gneissic Complex (CGC) of eastern Indian shield. The E-W trending mafic dykes from the Saltora area in the southeastern CGC underwent metamorphism in two episodes: M_1 (650 MPa; 770°C) and M_2 (300 MPa; 744°C). The metamafics are enriched in LILE, depleted in HFSE, and display strong fractionation of LREE, nearly flat HREE patterns in a chondrite-normalized REE diagram, and show tholeiitic differentiation trend. Their geochemical affinity is towards rift-related, continental within-plate basalts. About 7%–10% melting of the carbonated spinel-peridotite sub-continental lithospheric mantle (SCLM) produced the parental mafic magma. The pre-existing SCLM was metasomatized by slab-derived fluid during the previous subduction. The upwelling of the asthenosphere in a post-collisional tectonic setting caused E-W trending fractures, lithospheric thinning, and gravitational collapse. These dykes were emplaced during crustal extension around 1070 Ma. The remarkable geochemical similarity between the mafic dykes of Saltora and Dhanbad, the ca. 1096 Ma Mahoba (Bundelkhand craton), and the ca. 1070 Ma Alcurra mafic dykes in Australia supports a genetic link.

1. Introduction

Distinguishing high-grade mafic-ultramafic rocks crystallised originally from within-plate basaltic magmatism is challenging and crucial. The chemical composition of the igneous rocks gets modified during high-grade metamorphism, causing misidentification of the characters of the parental magma. Within-plate basaltic magma constitutes continental flood basalt provinces, oceanic plateaus, ocean basin flood basalts, continental rift valleys, giant dolerite dyke swarms in shield areas, layered mafic-ultramafic intrusions, and silicic and bimodal volcanic/plutonic provinces. Many authors consider the mafic dyke swarms as the feeder systems of deeply eroded Proterozoic Large Igneous Provinces and mantle plume activity (Ernst RE and Buchan KL, 2001; Evans DAD, 2013; Ernst RE, 2014; Mamouda A et al., 2022). Within-plate basaltic magmatism occurs during supercontinent breakup, too (Le Cheminant AN and Heaman LM, 1989; Ernst RE and Buchan KL, 2001).

Various Precambrian continental cratons merged to form the Rodinia supercontinent between 1300 Ma and 900 Ma (Li ZX et al., 2008; Xie HZ et al., 2023). The core cratons of the Rodinia were sutured by several Mesoproterozoic orogenies, including the Grenville orogenic belt (Hu Y et al., 2022). Even before the final assembly of the Rodinia, global, intracontinental magmatic events occurred at around 1100 Ma (Unrug R, 1996). The Mid-Continental Rift in Canada-USA, the Ngaanyatjarra Rift in Central Australia, the Umkondo LIP in southern Africa, the Southwestern USA Diabase Province, the Bahia Province in Brazil, and the Laanila-Kautokeino mafic dykes in the Fennoscandian shield all point to an intracontinental global magmatic event that happened at

First author: *E-mail address*: poulami.roy89@gmail.com (Poulami Roy).

* Corresponding author: *E-mail address*: bapigoswami69@gmail.com (Bapi Goswami).

Literary editor: Li-qiong Jia
doi:10.31035/cg20220082
2096-5192/© 2025 China Geology Editorial Office.

around 1100 Ma before the assembly of the Rodinia supercontinent (Evins PM et al., 2010). These intracontinental rifts provide critical records of tectonic conditions within continents during significant tectonic episodes (Elling R et al., 2022). Rift zones can also have abundant hydrocarbon reserves and provide the perfect conditions for diverse mineralization. Therefore, understanding rift mechanisms and structure aids our efforts to comprehend the nature of the continental lithosphere.

However, the characterization and correlation of Proterozoic magmatism are problematic because of the limited preservation of the supracrustal parts of the magmatic system and modification by later tectonic events. Despite this, we can compare the geochemistry of metamafic rocks across terranes to establish a chemical correlation. Knowing geochemistry cannot establish a connection, but significant contrasts in geochemical signatures can eliminate a correlation.

The Chhotanagpur Gneissic Complex (CGC) is a part of the 1500 km long Satpura Orogenic Belt in the eastern Indian Shield (Holmes A, 1955; Krishnan MS, 1961). The Satpura Orogenic Belt represents a collisional orogen, marking the Grenvillian amalgamation (1100–1000 Ma) of the South and North Indian cratons (Radhakrishna BP, 1989; Acharyya SK, 2003; Naganjaneyulu K and Santosh M, 2010; Bhowmik SK et al., 2012; Goswami B and Bhattacharyya C, 2014; Sequeira N et al., 2020; Fig. 1a). Several mafic dykes occur in the CGC, stretching from Central to Eastern India (Fig. 1a). These dykes strike toward ENE–WSW to E–W following the dominant structural trend of the region. Many authors studied the petrological and geochemical aspects of these dykes of the CGC (e.g., Kumar A and Ahmad T, 2007; Srivastava RK et al., 2012; Ghose NC and Chatterjee N, 2008; Bhattacharya DK et al., 2010). Srivastava RK et al. (2012) assigned Mesoproterozoic age for these mafic dykes. Kumar A and Ahmad T (2007) reported the petrography and geochemistry of the amphibolite dykes from Dhanbad. They proposed an enriched mantle source and a rift-setting for the emplacement of these dykes. Emplacement of the parental magma of amphibolite dykes from Deoghar likewise occurred during lithospheric extension (Mukherjee S et al., 2018). Kumar D et al. (2022) recently demonstrated that the amphibolite dykes formed in a post-collisional intra-continental extensional tectonic setting in the western part of the CGC at around 950 Ma. Ghose NC et al. (2005) voiced an intracratonic tectonic setting of the metamafics of CGC from south of the Damodar valley.

In this paper, we present new petrological and petrochemical data on the metabasic dykes of the Saltora area from the CGC (Figs. 1b, c) and hence the petrogenesis and geodynamical implications of these mafic dykes. These mafic intrusives show cross-cutting relation with the S_2-fabric of its basement. This study will also shed light on the mantle composition below the CGC during the end of the Mesoproterozoic. We will also compare the geochemical characteristics of these mafic intrusives with the dykes from adjacent Bundelkhand craton (1096±19 Ma) and mafic dykes of Ngaanyatjarra Rift, west Musgrave Province, Central Australia (1085–1040 Ma; Evins PM et al., 2010; Aitken AR et al., 2013) assuming all these dykes belong to a similar age.

2. Geological background

The CGC is dominantly composed of migmatites and felsic gneisses with older enclaves of metapelites, calc-silicate rocks, and metamafics (Ghose NC, 1983; Mazumdar SK, 1988; Mahadevan TM, 2002; Sanyal S and Sengupta P, 2012). Porphyritic granite, anorthosite, alkaline rocks including nepheline syenite, and mafic-ultramafic rocks occur as younger intrusives (Roy AK, 1977; Goswami B and Bhattacharyya C, 2008, 2010; Basak A et al., 2019, 2020; Roy P et al., 2020). Multiple generations of mafic intrusives reported from several places of CGC show concordant relation with the regional foliation (Sharma RS, 2009) (Fig. 1b).

The rocks of the CGC experienced at least two episodes of tectonothermal events during Proterozoic (Acharyya SK, 2003). The older enclave suites of CGC show variable degrees of metamorphism ranging from greenschist (SE part) to granulite facies (central and eastern parts of the terrain) (Mahadevan TM, 2002). The earliest high-temperature granulite-facies metamorphic event (M_1) occurred in the CGC at ca. 1650–1550 Ma (Acharyya SK, 2003; Chatterjee N et al., 2008; Dey A et al., 2019). Subsequently, at around 1450 Ma, A-type granitoids/ charnockites intruded the older gneisses of the CGC (Mukherjee S et al., 2017; Ray Barman T et al., 1994). Afterward, a second high-pressure granulite-facies metamorphism (M_2) took place ca. 1000–900 Ma (Maji AK et al., 2008; Dey A et al., 2019; Chatterjee N, 2018). A clockwise P–T path with a steep decompressive retrograde segment suggests continent-continent collision during the M_2-metamorphic event (Karmakar S et al., 2011; Rekha S et al., 2011; Goswami B and Bhattacharyya C, 2014; Mukherjee S et al., 2018).

2.1. Geology of the Saltora area

The Saltora area lie in the eastern part of the CGC. Roy AK (1977), Bhattacharyya PK and Mukherjee S (1987), Sen SK and Bhattacharya A (1986, 1993), Chatterjee N et al. (2008), Goswami B and Bhattacharyya C (2008), Maji AK et al. (2008), and Goswami B et al. (2018) described the geology of the area. Grey-colored biotite granitoid gneiss, often garnetiferous, is the major component of the migmatitic granitoid gneisses country of the Saltora area (Fig. 1c). Lensoidal enclaves of enderbite/charnoenderbite, migmatitic enderbite, khondalite, and calc-granulites occur within the migmatitic granitoid gneisses. The metasedimentary enclaves show gradational contact with the migmatitic granitoid gneiss. Long axes of the enclaves are aligned parallel to the regional foliation. Mafic granulites appear as older enclaves within the migmatitic granitoid gneisses (Bhattacharyya PK and Mukherjee S, 1987) and enderbites (Fig. 2a). These mafic granulites are co-folded with the country-rock gneisses (Figs.

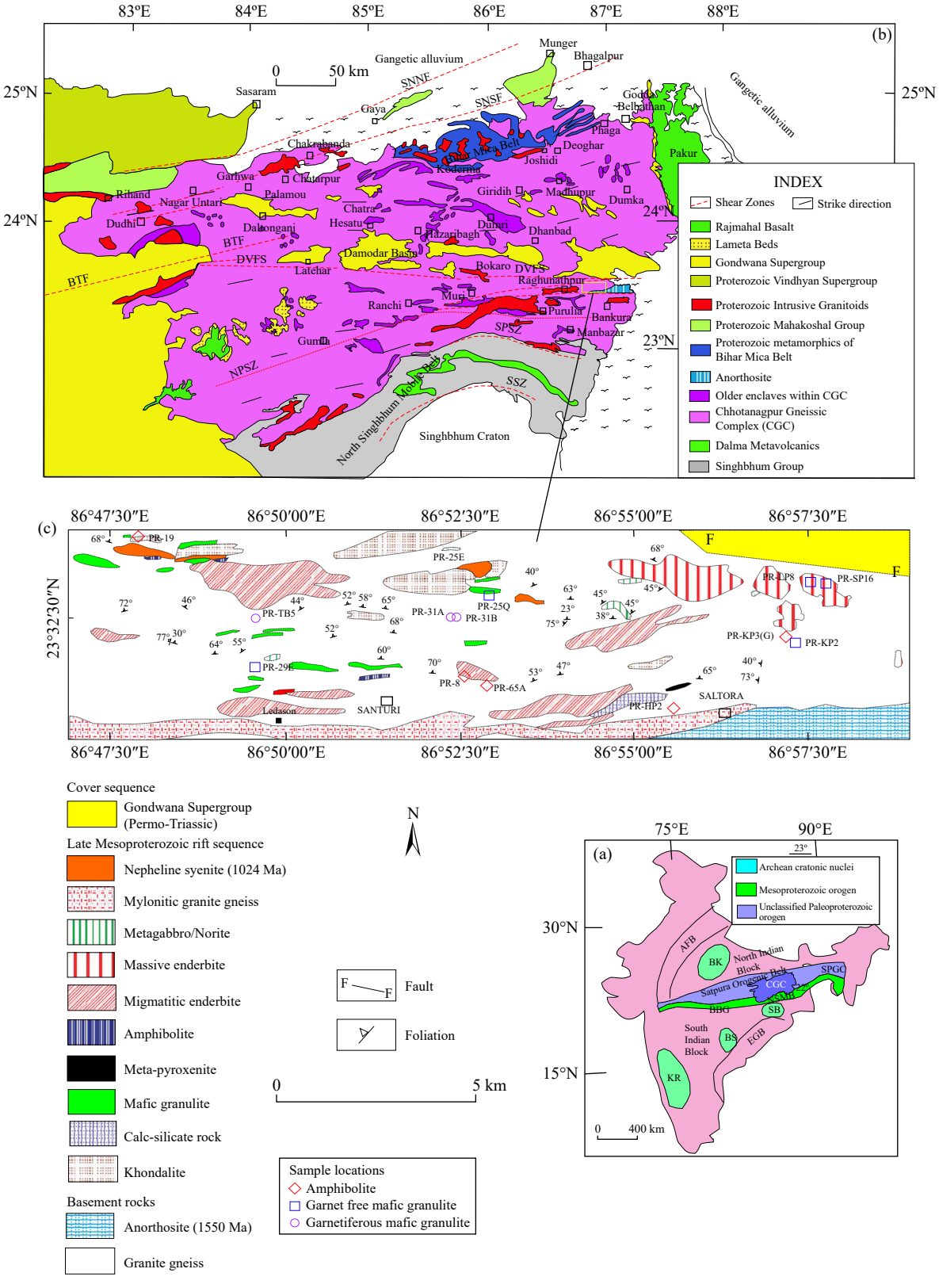

Fig. 1. (a) Map showing the disposition of the major cratonic blocks and tectonic elements within Peninsular India. AFB–Aravalli Fold Belt; BBG–Bhandara-Balaghat granulite; CGC–Chhotanagpur Gneissic Complex; NSMB–North Singhbhum Mobile Belt; EGB–Eastern Ghats Belt; RKG–Ramakona-Katangi granulite; SPGC–Shillong Plateau Gneissic Complex. Archaean cratons: BK–Bundelkhand; BS–Bastar; KR–Karnataka, SB–Singhbhum. (b) Generalized geological map of the Chhotanagpur Gneissic Complex, showing the distribution of major granitoid plutons and lineaments (modified from Mazumdar SK, 1988). SSZ– Singhbhum Shear Zone; SPSZ–South Purulia Shear Zone; NPSZ–North Purulia Shear Zone; SNNF–Son-Narmada North Fault; SNSF–Son-Narmada South Fault; BTF–Balarampur-Tatapani Fault; DVSF–Damodar Valley South Fault. The area of study is marked by the rectangle, lying north-east of Purulia town. (c) Simplified geological map around Santuri-Saltora area, Purulia and Bankura districts, West Bengal, India after Roy AK (1977), Acharya A et al. (2005) and modified by the present authors.

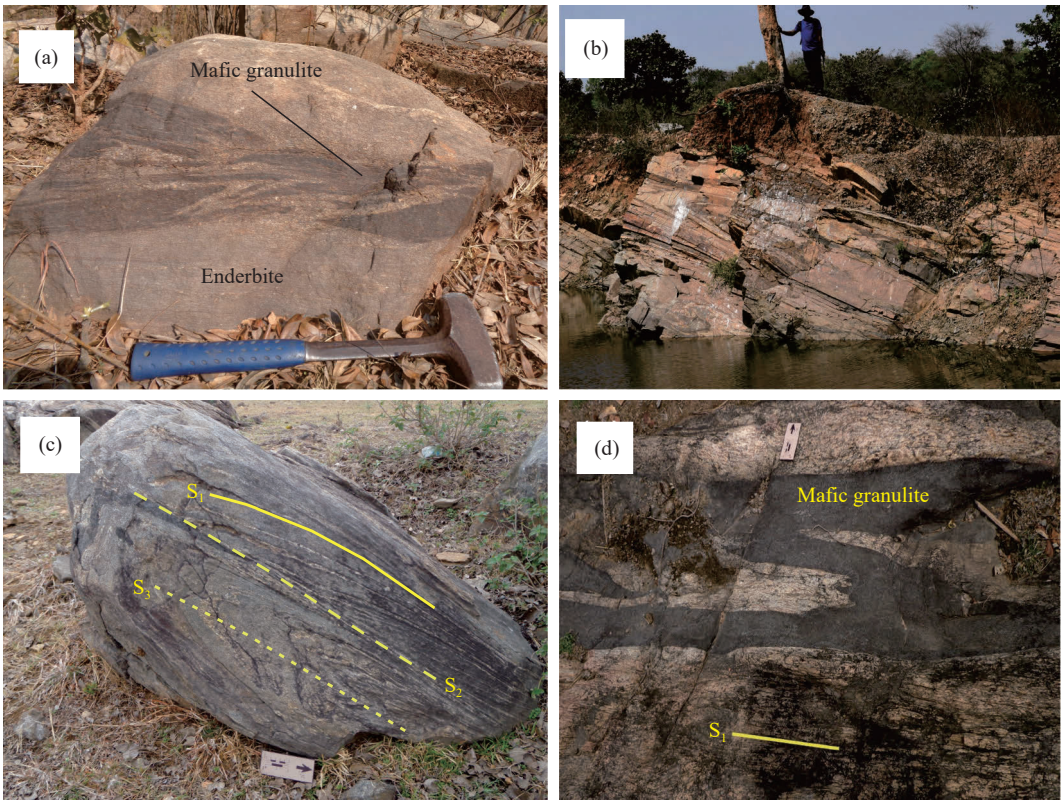

Fig. 2. Field photographs: (a) mafic granulites occurring as enclave within enderbite, Sarpahari, 4 km NNE of Saltora town. (b) Overturned D_2-antiform in the migmatitic granite gneiss, quarry section, Murlu, 3 km west of Saltora town. (c) Overturned D_2-antiform in the mafic granulite, north of Murlu. (d) Mafic granulite showing cross-cutting relation with the granite gneiss, quarry section, Murlu. Length of white scale = 14 cm.

2b–c). In contrast, some mafic granulites show cross-cutting relation within the country-rock gneisses (Fig. 2d).

The metasediments and migmatitic gneisses exhibit three phases of deformations (D_1, D_2, and D_3) (Roy AK, 1977; Chatterjee N et al., 2008; Goswami B and Bhattacharyya C, 2010; 2014). S_1 remains the dominant foliation of the area and axial planar to the isoclinal, rootless D_1-folds. D_1-folds rarely occur within intrafolial layers of migmatitic granitoid gneisses, quartzite, and calc-silicate rocks. The dominant foliation (S_1) of the area trends E–W to NE–SW with a low-to-moderate northerly dip (20°–40°) (Fig. 2a).

D_2-deformation folded the gneissic banding (S_1). D_2-folds are tight to close, low plunging with nearly E−W axial plane, and overturned southern limbs of the antiforms (Fig. 2a–b). Fracture cleavage (S_2), axial planar to the D_2-fold developed locally (Fig. 2b). The Saltora anorthosite pluton of the area emplaced synkinemetically during the D_2-deformation (Roy AK, 1977; Bhattacharyya PK and Mukherjee S, 1987). The shear movement along the North Purulia Shear Zone (NPSZ) represents the D_3-deformation. D_3-shear planes are E-W to ENE-WSW trending. Granite mylonites, augen gneisses, and leptynites form all along the NPSZ. Ribbon-quartz is omnipresent in the unmappable leptynites.

Metamorphic pressure and temperature conditions for the granulite facies M_1-metamorphism of the Saltora area were 750°C–850°C and 400 MPa to 600 MPa at >1.4 Ga (Maji et al., 2008). However, Chatterjee N et al. (2008) suggested granulite facies metamorphism (M_2) around Saltora attained 850 MPa to 1100 MPa and 850°C–900°C at 947±27 Ma. Karmakar S et al. (2011) suggested Mg-Al granulites and surrounding migmatitic gneisses lying south of Saltora area metamorphosed (M_2) at 870°C and1100 MPa, followed by a steep isothermal decompression to 600 MPa ca. 990–940 Ma.

The studied mafic dykes show cross-cutting relation with S_2-foliation of the granite gneisses country rocks (Fig. 2c) but subsequently deformed during the D_3-deformation.

3. Sample selection and analytical technique

In this study, fresh and representative samples were systematically collected both from isolated outcrops and exposures occuring as enclaves within the gneissic country. A total number of 50 samples were collected weighing a minimum of 5 kg each from the Saltora sector of Purulia-Bankura districts, West Bengal. Out of these hand specimens, approximately 40 samples were selected for making polished thin sections for microscopic identifications. Modal analysis of 31 representative samples (11 amphibolite and 20 mafic granulite) were performed by a point counter under 10.1 objective lens by counting 1000 points per slide. After detailed petrographic study, 5 amphibolite samples and 10 mafic granulite samples were selected for geochemical analysis. 2 amphibolite samples and 3 mafic granulite samples were selected for mineral chemistry by Electron Probe Micro Analysis.

Approximately 5 kg of sample material was ground to 0.5

Table 1. Modes (vol%) of the amphibolite and mafic graulites in Saltora area.

Type	Amphibolite												Garnet-free mafic granulite				
Sl No.	**1**	**2**	**3**	**4**	**5**	**6**	**7**	**8**	**9**	**10**	**11**		**12**	**13**	**14**	**15**	**16**
Sample	PR48	PR51	PR53	PR96	PR KP3(G)	PR 19	PR HP2	PR63	PR KP1	PR 65A	PR 62		PR KP2	PR 25E	PR 25Q	PR 37A	SP 16
Latitude (North)	23°31′	23°31′	23°31′	23°31′	23°31′	23°34′	23°31′	23°31′	23°31′	23°31′	23°31′		23°31′	23°33′	23°33′	23°31′	23°33′
	21.77″	20.81″	22.44″	08.39″	39.52″	00.13″	34.02″	07.24″	38.83″	08.39″	06.84″		35.16″	2.1″	05.25″	11.2″	12.69″
Longitude (East)	86°53′	86°53′	86°53′	86°52′	86°57′	86°47′	86°55′	86°52′	86°57′	86°52′	86°52′	**Av. (N=11)**	86°57′	86°52′	86°52′	86°56′	86°52′
	01.80″	04.65″	04.54″	48.70″	11.63″	38.93″	24.53″	46.78″	11.14″	48.70″	46.40″		40.55″	40.44″	40.74″	29.7″	53.72″
Quartz	1.6	0.1	1	1.4	2.8	1	3.1	2.4	5.2	9.3	8.9	3.35	0.3	0.3	6.2	7	0.3
Plagioclase	25.8	32.5	42.8	46.9	27.2	49.1	59.2	36.7	30.9	46.4	48.6	40.55	58.8	45	60.4	60.2	77.5
Hornblede	59.8	58.8	44.6	37.2	64.2	45.2	23.2	48.1	53.9	39.1	37.4	46.5	19.2	29.3	18.8	0	0
Biotite	0	5.2	0.3	0	0	0	0.5	0	0	0	0	0.55	10.2	0	0	10	0.3
Orthopyroxene	5.5	1.2	3.5	5.2	0	0	0	3.8	0	0	2.3	1.95	10.3	23.4	5.3	18.7	10.8
Cliopyroxene	6.9	1.3	4.2	4.3	5.3	4.2	13.5	6.8	8.5	4.5	2.5	5.64	0	0	6.9	3.7	9.9
Garnet	0	0	2.4	4	0	0	0	1.7	0	0	0	0.74	0	0	0	0	0
Opaque	0.4	0.1	1.2	1	0.5	0.5	0.5	0.5	1.5	0.7	0.3	0.65	0.5	2	2.4	0.4	1.2
Epidote	0	0.8	0	0	0	0	0	0	0	0	0	0.07	0	0	0	0	0
Apatite	0	0	0	0	0	0	0	0	0	0	0	0	Tr	0	Tr	0	Tr
Total	100	100	100	1200	100	100	100	100	100	100	100	100	99.3	100	100	100	100
Type	Garnet-free mafic granulite																
Sl no.	**17**	**18**	**19**	**20**	**21**	**22**	**23**	**24**	**25**	**26**	**27**	**28**		**29**	**30**	**31**	
Sample	LP 8	PR 29E	PR3	PR1	PR16	PR DS1	PR 25R	PR 30G	PR 25C	PR 101	PR 133	PR 103		PR TB5	PR 31B	PR 31A	
Latitude (North)	23°33′	23°31′	23°31′	23°31′	23°33′	23°31′	23°33′	23°31′	23°33′	23°32′	23°31′	23°31′		23°32′	23°34′	23°32′	
	30.06″	26.34″	35.04″	32″	12.69″	40.73″	02.77″	53.40″	12.42″	03.22″	50.98″	53.75″		41.18″	14.28″	15.06″	
Longitude (East)	86°57′	86°47′	86°45′	86°44′	86°52′	86°50′	86°52′	86°52′	86°52′	86°52′	86°52′	86°52′	**Av. (N=17)**	86°49′	86°52′	86°47′	**Av. (N=3)**
	17.79″	38.93″	29.62″	56.87″	53.72″	00.70″	40.77″	27.78″	52.86″	35.89″	27.99″	27.67″		22.11″	7.62″	10.38″	
Quartz	1	5.2	0	1.1	0.3	0	0	0	0.3	4	7.9	9.6	2.56	6.4	0	0	2.1
Plagioclase	48.5	70.1	61.7	64.1	78.2	47.3	40.8	48.6	48.7	49.3	56.7	62.1	57.53	74.1	37.6	30.1	47.3
Hornblende	31.3	0	26.1	0	0	19.6	0	26.2	31.1	27.3	11.3	0	14.13	0.5	27.3	25.7	17.8
Biotite	0	4	0	17.8	0	6.2	15.6	0.2	0.6	1.1	6.2	3.9	4.48	2.2	1.8	1.3	1.8
Orthopyroxene	17.1	8.3	0.6	7.8	5.8	25.6	39.1	24.2	17.3	4.3	7.7	8.8	13.83	8.5	20.1	35.2	21.3
Clinopyroxene	1.1	10.8	10.3	4.6	13.6	0.7	0.7	0	0.7	12.5	6.6	9.5	5.39	3.8	1.1	1.1	2.0
Garnet	0	0	0	0	0	0	0	0	0	0	0	0	0	3.5	5.6	5.5	4.9
Opaque	1	1.6	1.3	4.6	2.1	0.5	3.6	0.8	1.3	1.5	3.6	4.4	1.93	1	6.5	1.1	2.9
Epidote	0	0	0	0	0	0	0	0	0	0	0	0.2	0.01				
Apatite	0	Tr	0	0	Tr	0	0.1	0	0	0	0	1.5	0.13				
Total	100	100	100	100	100	99.9	99.9	100	100	100	100	100	99.99	100	100	100	100

mm in a steel-lined jawbreaker. By manually cone-and-quartering the crushed material, a subsample of 50 g was obtained. This 50 g sample was then pulverised to 200 mesh in an agate-lined ring-and-puck swing mill. Following that, 4 mg of powdered sample material was measured and mixed with binder boric acid using a mortar. The ratio of sample to boric acid should be 4∶1. The mixture was then placed in an aluminium cup and pressed for 20 seconds at a pressure of 20 ton. The pellet was then prepared for X-ray fluorescence (XRF) analysis.

Major element concentrations of 8 representative samples (7 basic granulite and 1 amphibolite) were determined by XRF at Presidency University, Kolkata, and using AXIOS of PANalytical Wavelength Dispersive X-ray fluorescence instrument with a flow scintillation detector. International certified reference material BHVO-1 was run as an internal check standard. Analytical uncertainties were < 5%.

Major and trace elements of 7 more samples (3 basic granulite and 4 amphibolite) were analyzed with a WDXRF S8 Tiger (4 kW) from Bruker-AXS, Germany, at the Department of Earth Sciences, IISER, Kolkata. Certified reference material BHVO-2 was used to validate results. The error in major- and trace-element analysis by XRF was estimated as < 2% and 5% respectively.

The concentrations of trace elements, including rare earth elements (REE), were determined using high-resolution inductively coupled plasma mass spectrometry (HR-ICP-MS) on a Perkin Elmer SCIEX ELAN DRC II instrument at the National Geophysical Research Institute in Hyderabad. The trace elements (including REE) were analysed by dissolving the sample powders and then digesting them in a closed vessel.

For trace element analyses, 0.05 g of fine powder sample (200 mesh) mixed with 10 mL of an acid mixture (7% HF: 3% HNO_3) was taken in clean savillex and kept in a hot plate at about 150°C for not less than 48 hours. Following this, the savillex was opened, and one drop of $HClO_4$ was added. The savillex was then kept on the hot plate for evaporation at about 150°C for 1 hour until almost dry. The remaining residue was dissolved by adding 10 mL 1∶1 HNO_3. This solution was supported on a hot plate for 30–40 minutes at ca. 80°C to dissolve all the suspended particles. Following this, the solution was transferred into a 250 mL flask, and 10 mL 1∶1 HNO_3 and Rhodium were added. ^{103}Rh was used as an internal standard. Millipore water was then added to top the volume up to 250 mL. Ultimately, the solution was stored in a polyethylene bottle. A 5 mL sample of this final solution was subsequently taken, and the volume was made up to 50 mL utilizing Millipore water. This solution was stored in a clean Eppendorf tube for HR-ICP-MS analysis. International certified reference material BHVO-1 was used as standard reference material. The relative deviations were < 5%.

4. Results

4.1. Petrography

Modes of the 11 amphibolites, 17 garnet-free mafic granulites and 3 garnetiferous mafic granulites are given in Table 1.

4.1.1. Amphibolite

These are coarse-grained, strongly schistose rocks, composed predominantly of brown/green Hbl and Pl, with subordinate Di, minor Qtz, ±Hyp, ±Bt, ±Grt, ±Ep, and Opq (mineral abbreviations after Whitney DL and Evans BW, 2010). Hbl (strongly pleochroic from brownish yellow to reddish brown) occurs as coarse, subidiomorphic, elongate plates and lensoid subhedra (Fig. 3a), defining distinct schistosity. Generally, it forms clusters that run following the elongate boundaries of Pl. It contains inclusions of sub-rounded to almost round Pl and fine Opq. Pl occurs as coarse, subidiomorphic, slightly elongated grains. The general elongation of the stumpy laths is parallel to the schistosity. However, Pl laths may exhibit a relict criss-cross arrangement (Fig. 3a). Tabular Pl shows bending of twin lamellae and marginal granulation. Di (pale green, non-pleochroic) and Hyp (pleochroic from pale pink to pale green) occur as medium-sized, subidiomorphic elongated grains and aggregates, intimately associated with hornblendes. The presence of Hyp indicates granulite facies metamorphism. Hbl and Bt replace pyroxenes (Fig. 3b). Di may occur as inclusions in coarser Pl. Medium to fine-sized, subidiomorphic Px appears intermittently in the interstitial space of Pl aggregates. Opq occurs as medium-sized, idiomorphic to subidiomorphic, equant to elongate grains generally associated with ferromagnesian silicates. The elongate opaques show parallelism with schistosity. Occasionally it occurs as extremely thin, lenticular inclusions oriented along a particular direction in some coarser hornblendes. Qz occurs as medium-sized xenoblastic grains interstices of fsp and fsp-ferromagnesian minerals.

4.1.2. Mafic granulites

These are dark-colored, apparently massive rocks, but under the microscope, the strong parallelism of almost all the principal minerals remains characteristic and impart a gneissosity. The impersistant layers of ferromagnesian minerals run almost alternately with clusters of elongate plagioclases. These rocks are predominantly composed of Pl, Hyp, Cpx, brownish Hbl, Bt, Opq, and Ap ± Grt. Based on mineralogy, the studied mafic granulites are divided into two groups: (1) garnetiferous, and (2) garnet-free mafic granulite.

Sub-idioblastic to xenoblastic, mostly elongated Pl shows preferred orientation along a particular direction. The grains frequently develop aggregates in which a reasonable number of grains are aligned slightly transverse to the general direction of the preferred orientation. Larger Pl may show deformation features, like shadowy extinction, bending of twin lamellae, and marginal granulation (Fig. 3c). Thin mafic veins often traverse through the Pl. Pools of Pl may run parallel to the general gneissosity of the rock. Pl may show criss-cross arrangements (Fig. 3d). Elongate grains of Hyp (pleochroic from pale green to pale pinkish brown) are

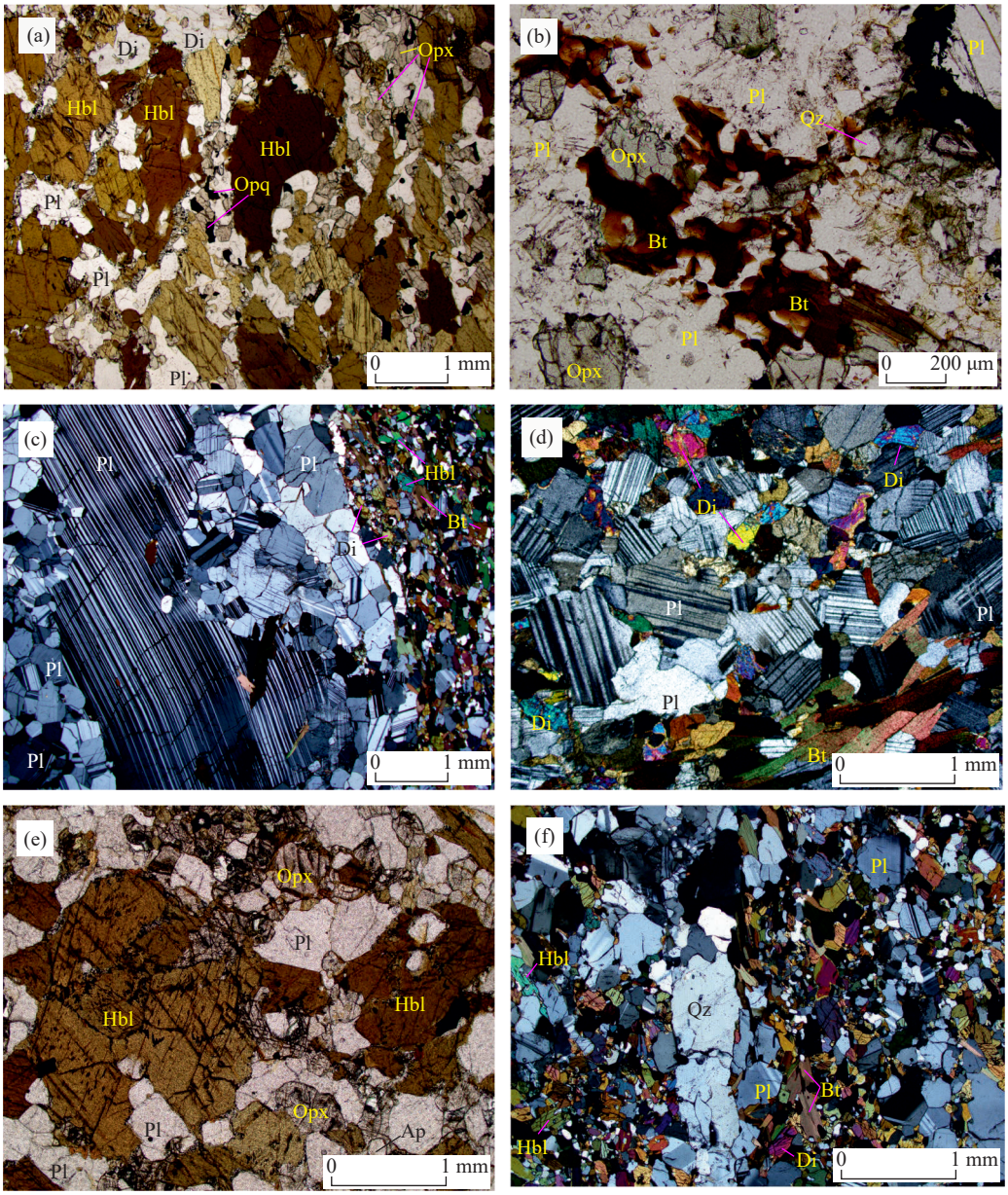

Fig. 3. Photomicrographs of amphibolite (a-b) and mafic granulite (c-f). (a) General schistose texture of brown Hbl-rich amphibolite. (b) Biotitization of Opx in amphibolite. (c) The megacrysts of Pl in mafic granulites show deformational features like shadowy extinction, bending of twin lamellae and marginal granulation to medium sized grains. (d) Tabular Pl occur as criss-cross aggregates within the ferromagnesian mineral aggregates. (e) Replacement of Opx by brown and greenish brown Hbl occasionally preserving Opx relicts in mafic granulite. Locally the plagioclase grains show preferred orientation along the general gneissosity in mafic granulite. (f) Coarse elongate Qz in gneissic mafic granulite runs parallel to the gneissic trend. (Mineral abbreviations after Whitney DL and Evans BW, 2010).

oriented, together with the Pl and other minerals, in the preferred direction of gneissosity. The grains are chiefly sub-idioblastic, but xenoblastic grains are equally common. Idioblastic grains are rare. Cpx (non-pleochroic, pale green) occurs as xenoblastic to sub-idioblastic grains associated with orthopyroxene and sporadic Hbl. Hbl typically replaces pyroxenes (Fig. 3e). Hbl (strongly pleochroic from greenish-yellow to brownish-yellow) occurs most commonly as sub-idioblastic to xenoblastic elongate grains showing preferred orientation with other minerals. Exsolved needles of opaques within yellow-brown Hbl show preferred orientation. Biotitization of Hbl is common (Fig. 3e). Grt (pale pinkish-brown) infrequently exists as minuscule, irregular inclusions within Pl. Medium- to fine-sized sub-idioblastic to xenoblastic Bt (pleochroic from dark-brown to yellowish-brown) occurs intimately associated with Px and Hbl. Opq appear as fine- to medium-sized laths, almost invariably associated with ferromagnesian minerals. Elongated grains are routinely parallel to sub-parallel with the long dimension of ferromagnesian minerals. A few opaque grains are skeletal. The grains are rarely present as inclusions in Pl. Ap is present as fine idiomorphic- to sub-idiomorphic inclusions in Pl and equally at the contact of plagioclase and ferromagnesian minerals. Qz, when present, may occur as coarse, lenticular grains that are strongly oriented parallel to the gneissic trend (Fig. 3f). It may equally occur as a medium- to fine-sized

grain interstitial to Pl and ferromagnesian minerals.

4.2. Mineral chemistry

The representative electron probe microanalyses (EPMA) of Pl, Kfs, Amp, Bt, Px, Grt, Ap, Ilm, and Mag (minerals abbreviations after Whitney DL and Evans BW, 2010) can be found in Supplementary Tables 1–10. Amphibolite plagioclases range from andesine to labradorite ($An_{34.80}$–$An_{67.10}$). Andesine ($An_{38.50}$–$An_{49.10}$) is the plagioclase composition of garnet-free mafic granulites. Pl compositions in garnetiferous mafic granulites, on the other hand, range from andesine to labradorite ($An_{49.20}$–$An_{64.00}$) (Supplementary Table 1; Supplementary Fig. 1a). The Or-component ($Or_{97.20}$) is abundant in the Kfs of mafic granulite (Supplementary Table 2; Supplementary Fig. 1a).

The amphiboles in amphibolites and mafic granulite are rich in calcium. The CaO content for amphibolite, garnet-free, and garnetiferous mafic granulite is 12.34%, 11.54%, and 11.53%, respectively (Supplementary Table 3). According to the IMA classification scheme, the amphiboles range from magnesio-hestingsite to ferro-pargasite (Supplementary Fig. 1b, c). Bt are moderately enriched in Mg, with a Mg/(Mg+Fe) ration of about 0.51 for amphibolite, 0.46 for garnetiferous mafic granulite, and 0.45 for garnet-free mafic granulite. According to the classification scheme of Deer WA et al. (1992), all the analysed Bt are plotted within the biotite field (Supplementary Fig. 1d). Opx are ferrosilite, while Cpx are diopside (Supplementary Fig. 1e). Opx has a FeO content of 33.27% (garnetiferous mafic granulites) and 31.40% (garnet-free mafic granulites) (Supplementary Table 5). The FeO(t) contents of the Cpx (Di) analysed from amphibolites ranges from 9.21% to 12.28% and in garnet-free mafic granulites it varies from 11.0% to 12.33% (Supplementary Table 6). Grt has an average composition of $Alm_{64.40}Sps_{2.33}Grs_{20.64}Prp_{12.43}$. These garnets have a low MnO content (1.04%; Supplementary Table 7). The P_2O_5 and CaO contents of the analysed apatite are approximately 41.70% and 55.51% in amphibolites, respectively. The P_2O_5 and CaO contents of the analysed apatite in mafic granulites are 40.80% and 56.84%, respectively (Supplementary Table 8). The average TiO_2 and FeO contents of Ilm in amphibolites are 50.15% and 45.01%, respectively, whereas Mag has a FeO content of 76.19%. The average TiO_2 and FeO contents of Ilm in garnet-free mafic granulites are 50.36% and 43.37%, respectively. The average TiO_2 and FeO contents of Ilm in garnetiferous mafic granulites are 50.19% and 43.67%, respectively.

4.3. Major and trace element geochemistry

Major and trace element concentrations of 15 representative samples (5 samples of amphibolites, 7 samples of garnet-free mafic granulites, 3 samples of garnetiferous mafic granulites) from the study area are presented in Table 2.

The amphibolites have moderate contents of SiO_2 (av. 50.68%), high MgO (av. 6.24%), and Al_2O_3 (av. 16.55%), high contents of $Fe_2O_3^T$ (av. 9.97%), low K_2O (av. 0.81 wt. %) and (K_2O + Na_2O) (av. 3.70%) with high Na_2O/K_2O ratios (av. 4.03). The average Mg# of the amphibolites is about 59.38.

The garnet-free mafic granulites have slightly higher concentrations of SiO_2 compared to the garnetiferous variety (about 50.65% and about 49.76%, respectively) and higher MgO (5.74% and 4.67%, respectively). The Al_2O_3 contents of the two varieties are 15.47% and 13.46%., respectively. The garnetiferous mafic granulite has relatively high $Fe_2O_3^T$ (16.42%) than the garnet-free varieties (about 11.78%). The Mg# of the Saltora mafic granulites shows a restricted range, varying from 39.56 (garnetiferous) to 52.77 (garnet-free).

In Harker-type variation diagrams, we plot major oxide and trace elements (Supplementary Fig. 2a–p) against MgO. The investigated samples show the negative correlations of MgO with SiO_2, Fe_2O_3(t), TiO_2, P_2O_5, and positive correlations with Na_2O and CaO. The correlation between MgO and K_2O, if any, is not clear. Rb, Sr, Nb, Y, and Ce show a negative correlation, while Cr and Sc exhibit a positive correlation with MgO. For Yb, there is random distribution against MgO.

The studied samples show negative correlations of Zr with P_2O_5, Co, and Sc and a positive correlation with TiO_2, Fe_2O_3, MgO, CaO, and Rb with Zr (Supplementary Fig. 3a–l).

In the Nb/Y vs. Zr/Ti diagram (after Pearce JA, 1996), both amphibolites and mafic granulites show a basaltic composition, while only three samples are plotted in the andesite-basaltic andesite field. One garnetiferous mafic granulite falls in the alkali basalt field, and one amphibolite was is plotted in the foidite field (Fig. 4a).

In the total alkali vs. SiO_2 diagram (after Cox K et al., 1979), most of the samples were plotted in the basalt field, while two samples (garnetiferous and garnet-free mafic granulite, one each) are plotted in the basaltic andesite field, the other two samples (one amphibolite and one garnet-free mafic granulite) lie in the andesite field (Fig. 4b).

On the ternary (FeO^T+TiO_2)–Al_2O_3–MgO diagram, eleven samples lie within the basalt field, and two amphibolites and one garnet-free mafic granulites lie in the andesite to basalt field (Fig. 4c).

In the AFM ternary diagram (Irvine TNJ and Baragar WRAF, 1971), most of the samples plot within the tholeiitic field, and only two samples of amphibolite and two samples of garnet-free mafic granulite plot within the calc-alkaline field but very near to the tholeiitic field (Fig. 4d).

Total REE contents of amphibolites, garnet-free mafic granulites and garnetiferous mafic granulites are av. 43.50×10^{-6}, 52.90×10^{-6}, and 100.16×10^{-6}, respectively. The $(Ce/Yb)_N$ (normalized by C-1 Chondrite values of McDonough WF and Sun SS (1995) ratios of amphibolites, garnet-free mafic granulites, and garnetiferous mafic granulites are 4.97, 3.10, and 3.24 respectively. Chondrite-normalized REE diagram (normalized by C-1 Chondrite values of McDonough WF and Sun SS (1995) of the mafic granulites is shown in Fig. 5a. The HREE patterns of the studied samples are almost flat. The studied mafic granulites

exhibit weak-negative to slightly positive Eu-anomalies. In the Primitive-Mantle normalized multi-element spider diagram (normalization values after Sun SS and McDonough WF, 1989), the mafic granulites show a highly positive Pb anomaly, a moderately positive anomaly of Ba, and low negative anomalies of Ce, Sr and Zr (Fig. 5b). The amphibolite shows highly fractionated LREE and HREE patterns in the Chondrite-normalized REE diagram (normalized by C-1 Chondrite values of McDonough WF and Sun SS, 1995) (Fig. 5c). In the Primitive-Mantle normalized multi-element spider diagram (normalization values after Sun SS and McDonough WF, 1989), amphibolite shows negative

Table 2. Major oxides (%) and trace elements (10^{-6}) concentrations of the amphibolites and mafic granulites in Saltora area.

Sample	PR 19	PR 8	PR KP3(G)	PR 65A	PR HP2	Av.	PR KP2	PR 25E	PR 25Q
Sl no	1	2	3	4	5	**(N=5)**	6	7	8
Rock type	**Amphibolite**						**Garnet-free mafic granulite**		
SiO_2	48.46	49.9	48.78	47.97	58.31	**50.68**	58.02	45.32	49.15
TiO_2	1.11	1.21	1.22	0.47	1.16	**1.03**	0.81	1.17	1.73
Al_2O_3	15.41	15.97	13.92	22.37	15.07	**16.55**	16.63	15.62	15.09
$Fe_2O_3^T$	11.59	11.27	13.17	7.12	6.72	**9.97**	7.58	12.1	14.77
MnO	0.164	0.177	0.211	0.12	0.06	**0.15**	0.11	0.16	0.19
MgO	7.434	7.83	6.737	5.39	3.82	**6.24**	3.96	8.59	5.22
CaO	12.65	10.64	10.79	13.64	7.82	**11.11**	7.03	12.43	11.4
Na_2O	2.11	2.38	2.98	2.71	4.29	**2.89**	3.81	1.55	2.75
K_2O	0.71	0.47	0.96	0.45	1.44	**0.81**	1.42	0.64	0.28
P_2O_5	0.09	0.151	0.131	0.08	0.53	**0.2**	0.18	0.14	0.18
Total	**99.79**	**99.99**	**98.89**	**100.32**	**99.22**	**99.63**	**99.55**	**97.72**	**100.76**
(Trace element in ppm)									
Cr	300.5	248.2	169.9	349.2	32.65	**220.09**	37.37	261.72	97.92
Ni	96.6	77.4	31.7	48.2	10.09	**52.8**	62.91	135.56	85.28
Co	37	34.6	40.5	26.3	62.09	**40.1**	69.02	75.19	79.57
V	247.3	214.6	263.8	117.6	164.78	**201.62**	141.18	252.06	393.25
Cu	0	35.5	75	12.9	2.37	**25.15**	67.56	67.17	188.36
Pb	3.7	4.8	4.9	0	63.35	**15.35**	3.9	4.95	3.28
Zn	80.6	77.3	87.7	66.2	41.48	**70.66**	155.25	64.97	158.69
Rb	10.5	9.7	9.9	15.5	55.21	**20.16**	43.65	8.13	2.66
Ba	28.8	112.4	73.4	11	560.59	**157.24**	292.9	126.88	150.74
Sr	119.2	153	94.2	203.3	419.3	**197.8**	400.99	200.03	212.84
Ga	17.5	18.9	17.9	14.9	28.51	**19.54**	19.56	16.63	19.32
Nb	10.6	10.6	10.6	7.9	15.56	**11.05**	6.5	4.88	9.14
Ta	0.2	0.4	0.3	0.6	1.26	**0.55**	1.06	0.55	0.94
Zr	176.95	359.31	122.92	49.6	105.55	**162.87**	84.05	53.84	50.81
Hf	4.2	3.7	2.9	1.3	3.07	**3.03**	2.08	1.56	1.7
Y	20	20	20	2	25.23	**17.45**	19.33	21.33	37.59
Th	1.6	1.9	2.2	1.5	4.81	**2.4**	1.02	0.4	0.33
Sc	42.9	34.8	44.4	23.6	16.61	**32.46**	19.66	39.42	46.82
Cs	–	–	–	–	0.91	**0.91**	0.58	0.27	0.1
U	4.2	4.2	4.2	4.8	1.52	**3.78**	0.29	0.09	0.16
La	–	–	–	–	41.86	**41.86**	16.85	5.32	9.67
Ce	0	20	10	1	85.86	**23.37**	36	13.18	23.82
Pr	–	–	–	–	10.91	**10.91**	4.57	2	3.48
Nd	–	–	–	–	46.49	**46.49**	17.87	9.06	15.54
Sm	–	–	–	–	9.92	**9.92**	3.68	2.59	4.27
Eu	–	–	–	–	2.16	**2.16**	1.12	1.04	1.5
Gd	–	–	–	–	6.56	**6.56**	3.69	3.31	5.54
Tb	–	–	–	–	1.09	**1.09**	0.56	0.57	0.97
Dy	–	–	–	–	4.77	**4.77**	3.14	3.49	6.04
Ho	–	–	–	–	0.9	**0.9**	0.64	0.76	1.31
Er	–	–	–	–	1.97	**1.97**	1.74	2.04	3.57
Tm	–	–	–	–	0.27	**0.27**	0.27	0.31	0.55
Yb	4	4.2	0	5.4	1.76	**3.07**	1.77	2.03	3.62
Lu	–	–	–	–	0.25	**0.25**	0.27	0.32	0.56
∑REE	**4**	**24.2**	**10**	**6.4**	**172.89**	**43.5**	**75.32**	**40.7**	**70.77**

Table 2-1. Continued.

Sample	PR 19	PR 8	PR KP3(G)	PR 65A	PR HP2	**Av.**	PR KP2	PR 25E	PR 25Q
Sl no	1	2	3	4	5	**(N=5)**	6	7	8
Rock type	**Amphibolite**						**Garnet-free mafic granulite**		
(Na_2O+K_2O)	2.82	2.85	3.94	3.16	5.73	**3.7**	5.23	2.19	3.03
(Na_2O/K_2O)	2.97	5.06	3.1	6.02	2.98	**4.03**	2.68	2.42	9.82
Mg#	0.6	0.6	0.5	0.6	0.6	**0.6**	0.5	0.6	0.5
S/(SAF)	0.64	0.65	0.64	0.62	0.73	**0.66**	0.71	0.62	0.62
$(Ce/Yb)_N$[$]	–	1.32	–	0.05	13.55	**4.98**	5.65	1.8	1.83
Eu/Eu*	–	–	–	–	0.27	**0.27**	0.3	0.36	0.31
Ce/Ce*					0.99	**0.27**	1.01	0.99	1.01
$(Ho/Yb)_N$[#]	–	–	–	–	1.53	**1.53**	1.09	1.12	1.09
Rb/Sr	0.09	0.06	0.11	0.08	0.13	**0.09**	0.11	0.04	0.01
Ba/Rb	2.74	11.59	7.41	0.71	10.15	**6.52**	6.71	15.61	56.67
Ba/La	–	–	–	–	13.39	**13.39**	17.38	23.85	15.59
Ba/Th	18	59.16	33.36	7.33	116.6	**46.89**	287.16	317.2	456.79
Pb/Ce	–	0.24	0.49	0	0.74	**0.37**	0.11	0.38	0.14
La/Nb	–	–	–	–	2.69	**2.69**	2.59	1.09	1.06
La/Yb	–	–	–	–	23.78	**23.78**	9.52	2.62	2.67
Nb/Y	0.53	0.53	0.53	3.95	0.62	**1.23**	0.34	0.23	0.24
Nb/La	–	–	–	–	0.37	**0.37**	0.39	0.92	0.95
Nb/Yb	2.65	2.52	–	1.46	8.84	**3.87**	3.67	2.4	2.52
Nb/Ta	53	26.5	35.33	13.17	12.32	**28.06**	6.15	8.86	9.69
ΔNb	-0.35	-0.94	-0.05	-0.34	0.34	**-0.27**	0.04	0.33	0.87
Zr/Nb	16.69	33.9	11.6	6.28	6.78	**15.05**	12.93	11.03	5.56
Th/Yb	0.4	0.45	–	0.28	2.73	**0.97**	0.58	0.2	0.09
Zr/Y	8.85	17.97	6.15	24.8	4.18	**12.39**	4.35	2.52	1.35
Zr/Hf	42.13	97.11	42.39	38.15	34.39	**50.83**	40.41	34.51	29.89
Th/Nb	0.15	0.18	0.21	0.19	0.31	**0.21**	0.16	0.08	0.04
Ti/V	26.9	33.8	27.72	23.96	42.2	**30.91**	34.39	27.82	26.37
Y/Ho	–	–	–	–	28.15	**28.15**	30.2	28.07	28.69
Y/Yb	5	4.76	–	0.37	14.33	**6.12**	10.92	10.51	10.38

$ Chondrite-normalized (Sun SS and McDonough WF, 1989) values. #Primitive-mantle normalized (Sun SS and McDonough WF , 1989) values.

Ba, Sr, Nb, and Ta anomalies but strongly positive Pb and U anomalies and moderately positive Zr anomaly (Fig. 5d). Although from a REE diagram of a single sample of amphibolite no definite inference should be made, it is noted its highly fractionated nature which is in conformity with 3 samples of mafic granulite (Fig. 5a, c).

5. Discussion

5.1. Post-crystallization alteration effects on whole-rock geochemistry

The meta-igneous rocks of the Saltora area had suffered granulite facies metamorphism. This high-grade metamorphism could have resulted in the mobility of some elements, rendering them useless for deciphering the primary petrogenetic processes. To avoid trace element partitioning on a local scale due to different mineral assemblages, fresh samples were carefully selected and large amount of sample specimens were crushed. In total, 15 samples are chosen to serve as the foundation for all subsequent discussions.

Several researchers believe that the metasomatic change of the granulite facies mafic rocks is insignificant due to their low permeability from the fluid conduits (e.g., Harlov DE, 2012). Moreover, if mafic rocks intrude the host gneisses during the waning phase of granulite facies metamorphism, they suffer little compositional change (Sharma RS et al., 1987). Weaver BL and Turney J (1981) have shown that mobility of trace elements during high-grade metamorphism is related to availability of the fluid phase. These authors suggested rare earth elements (REE) remained immobile during granulite facies metamorphism. Ghatak A et al. (2012) concluded mafic and ultramafic rocks in subduction zones preserve elemental compositions and isotope ratios during high-grade metamorphism. Several authors show that Rb, K, Ba, Sr, Pb, and Th show superior mobility while La, U, and Sr show lesser mobility during metamorphism (Weaver BL and Turney J, 1981; Ghatak A et al., 2012). In contrast, Ague JJ (2017) suggested partial mobility of HFSE of high-grade metamafic rocks. Babechuk MG et al. (2014) showed that U, Mo, and W remain the most mobile elements among the HFSEs, while Zr, Hf, Nb, and Ta maintain the ratios of the basalt protolith.

Most researchers (e.g., Polat A and Hofmann AW, 2003) consider the large-ion lithophile elements (LILE) as being easily mobilized during metamorphism or alteration

processes, whereas the high field strength elements (HFSE) and the rare earth elements (REE) are regarded as relatively immobile. The coherent patterns in the chondrite and primitive mantle normalized rare earth and trace element plots of the studied mafic granulites (Fig. 5) support this viewpoint.

Polat A et al. (2002) have established Ce/Ce* [$Ce/Ce^* = Ce_N/(La_N*Pr_N)^{0.5}$, chondrite normalized values after McDonough WF and Sun SS, 1995] ratios of rocks would vary between 0.9 and 1.1 during limited LREE mobility. The Ce/Ce* ratios in the studied samples vary from 0.99 to 1.05 suggesting the immobile behavior of LREE during metamorphism (Table 2).

Table 2-2. Continued.

Sample	PR 37A	PR SP 16	PR LP 8	PR 29E	**Av.**	PR TB5	PR 31B	PR 31A	**Av.**
Sl no	9	10	11	12	**(N=7)**	13	14	15	**(N=3)**
Rock type	**Garnet-free mafic granulite**					**Garnetiferous mafic granulite**			
SiO_2	48.38	49.23	49.42	55.02	**50.65**	53.53	48.39	47.35	**49.76**
TiO_2	1.65	1.9	1.05	1.32	**1.38**	3.13	2.15	1.87	**2.38**
Al_2O_3	15.69	13.98	15.85	15.41	**15.47**	12.75	14.07	13.57	**13.46**
$Fe_2O_3^T$	11.64	14.13	11.48	10.74	**11.78**	15.69	17.51	16.05	**16.42**
MnO	0.17	0.21	0.176	0.15	**0.17**	0.21	0.25	0.22	**0.23**
MgO	6.12	5.545	6.821	3.94	**5.74**	3.72	4.41	5.89	**4.67**
CaO	9.76	11	12.61	7.88	**10.3**	7.67	10.1	11.2	**9.66**
Na_2O	3.16	3.15	2.48	2.51	**2.77**	2.01	2.21	2.07	**2.1**
K_2O	1.47	0.37	0.58	1.59	**0.91**	0.36	0.29	0.38	**0.34**
P_2O_5	0.51	0.183	0.093	0.27	**0.22**	0.63	0.34	0.26	**0.41**
Total	**98.55**	**99.698**	**100.56**	**98.83**	**99.38**	**99.7**	**99.72**	**98.86**	**99.43**
(Trace element in ppm)									
Cr	49.2	48	126.8	92.48	**101.93**	26.63	20.27	47.39	**31.43**
Ni	13.6	15.7	49.6	41.88	**57.79**	9.93	56.07	64.07	**43.36**
Co	32.2	42.5	40.7	52.84	**56**	67.54	88.27	85.24	**80.35**
V	133.1	365.9	248.9	209.78	**249.17**	288.79	415.89	379	**361.23**
Cu	34	7.2	20.3	36.73	**60.19**	1.28	33.69	46.71	**27.23**
Pb	6.4	1.4	2.3	5.55	**3.97**	48.69	4.73	1.83	**18.42**
Zn	92.6	79	72.6	106.79	**104.27**	38.9	91.51	74.46	**68.29**
Rb	28.5	9.7	9.7	52.58	**22.13**	18.21	3.9	3.84	**8.65**
Ba	284.5	27.1	59.4	286.44	**175.42**	459.82	115.13	106.67	**227.21**
Sr	356.4	164.9	124.8	133.5	**227.64**	320.12	220.75	185.4	**242.09**
Ga	20.4	20.1	17.5	20.59	**19.16**	25.82	22.24	19.71	**22.59**
Nb	23.7	10.6	10.6	11.93	**11.05**	40.21	13.56	10.46	**21.41**
Ta	–	–	–	0.6	**0.79**	3.49	0.85	0.73	**1.69**
Zr	–	125.62	152.64	124.89	**98.64**	231.76	49.56	39.56	**106.96**
Hf	4.7	3.2	1.4	3.05	**2.53**	5.8	1.45	1.47	**2.91**
Y	30	30	20	36.74	**27.86**	35.87	42.36	37.65	**38.63**
Th	3.1	1.7	2.3	1.69	**1.51**	3.06	0.47	0.28	**1.27**
Sc	20.6	40.3	43.7	35.04	**35.08**	18.46	56.05	54.71	**43.07**
Cs	–	–	–	0.9	**0.46**	0.88	0.12	0.12	**0.37**
U	4.2	4.2	4.2	0.45	**1.94**	1.07	0.22	0.14	**0.48**
La	–	–	–	25.13	**14.24**	28.34	11.48	11.32	**17.05**
Ce	40	10	10	57.3	**27.19**	60.75	29.34	28.38	**39.49**
Pr	–	–	–	6.9	**4.24**	7.86	4.37	4.08	**5.44**
Nd	–	–	–	27.21	**17.42**	34.34	19.74	18.03	**24.04**
Sm	–	–	–	6.07	**4.15**	8.02	5.53	4.85	**6.13**
Eu	–	–	–	1.48	**1.29**	2.12	1.81	1.58	**1.84**
Gd	–	–	–	6.48	**4.76**	6.37	6.78	5.93	**6.36**
Tb	–	–	–	1.04	**0.79**	1.21	1.16	1.01	**1.13**
Dy	–	–	–	6.1	**4.69**	6	7.02	6.07	**6.36**
Ho	–	–	–	1.27	**1**	1.21	1.45	1.29	**1.32**
Er	–	–	–	3.45	**2.7**	2.95	3.97	3.46	**3.46**
Tm	–	–	–	0.53	**0.42**	0.44	0.61	0.53	**0.53**
Yb	0	0	1.6	3.55	**1.8**	3.12	3.95	3.5	**3.52**
Lu	–	–	–	0.54	**0.42**	0.48	0.61	0.54	**0.54**
∑REE	**40**	**10**	**11.6**	**121.92**	**52.9**	**134.89**	**86.34**	**79.25**	**100.16**

Table 2-3. Continued.

Sample	PR 37A	PR SP 16	PR LP 8	PR 29E	**Av.**	PR TB5	PR 31B	PR 31A	**Av.**
Sl no	9	10	11	12	**(N=7)**	13	14	15	**(N=3)**
Rock type	**Garnet-free mafic granulite**					**Garnetiferous mafic granulite**			
(Na_2O+K_2O)	4.63	3.52	3.06	4.1	**3.68**	2.37	2.5	2.45	**2.44**
Na_2O/K_2O	2.15	8.51	4.28	1.58	**4.49**	5.58	7.62	5.45	**6.22**
Mg#	0.6	0.5	0.6	0.5	**0.5**	0.4	0.4	0.5	**0.4**
S/(SFS)	0.64	0.64	0.64	0.68	**0.65**	0.65	0.61	0.62	**0.62**
Ce_N/Yb_N[$]	–	–	1.74	4.48	**3.1**	5.41	2.06	2.25	**3.24**
Eu*	–	–	–	0.24	**0.3**	0.3	0.3	0.29	**0.3**
Ce/Ce*				1.07	**0.86**	1.00	1.02	1.02	**1.01**
$(Ho/Yb)_N$[#]	–	–	–	1.07	**1.09**	1.17	1.1	1.11	**1.13**
Rb/Sr	0.08	0.06	0.08	0.39	**0.11**	0.06	0.02	0.02	**0.03**
Ba/Rb	9.98	2.79	6.12	5.45	**14.76**	25.25	29.52	27.78	**27.52**
Ba/La	–	–	–	11.4	**17.05**	16.22	10.03	9.42	**11.89**
Ba/Th	91.77	15.94	25.83	169.49	**194.88**	150.22	244.96	380.96	**258.71**
Pb/Ce	0.16	0.14	0.23	0.1	**0.18**	0.8	0.16	0.06	**0.34**
La/Nb	–	–	–	2.11	**1.71**	0.7	0.85	1.08	**0.88**
La/Yb	–	–	–	7.08	**5.47**	9.08	2.91	3.23	**5.07**
Nb/Y	0.79	0.35	0.53	0.32	**0.4**	1.12	0.32	0.28	**0.57**
Nb/La	–	–	–	0.47	**0.68**	1.42	1.18	0.92	**1.17**
Nb/Yb	–	–	6.63	3.36	**3.72**	12.89	3.43	2.99	**6.44**
Nb/Ta	–	–	–	19.95	**11.16**	11.52	15.99	14.37	**13.96**
ΔNb	–	0.09	-0.23	0.23	**0.22**	0.23	1.11	1.14	**0.83**
Zr/Nb		11.85	14.4	10.47	**11.04**	5.76	3.65	3.78	**4.4**
Th/Yb	–	–	1.44	0.48	**0.56**	0.98	0.12	0.08	**0.39**
Zr/Y	–	4.19	7.63	3.4	**3.91**	6.46	1.17	1.05	**2.89**
Zr/Hf	–	39.26	109.03	40.95	**49.01**	39.95	34.18	26.91	**33.68**
Th/Nb	0.13	0.16	0.22	0.14	**0.13**	0.08	0.03	0.03	**0.05**
Ti/V	74.31	31.12	25.29	37.72	**36.72**	64.97	30.99	29.57	**41.84**
Y/Ho	–	–	–	28.93	**28.97**	29.6	29.21	29.19	**29.33**
Y/Yb	–	–	12.5	10.35	**10.93**	11.5	10.72	10.76	**10.99**

Hill IG et al. (2000) introduced an index of alteration for the basaltic rocks defined by the $SiO_2/(SiO_2+Al_2O_3+Fe_2O_3t)$ (hereafter called the S/SAF ratio) and suggested that basaltic rocks with S/SAF ratio <0.5 show significantly altered HFSE contents. S/SAF ratios of the studied mafic granulites vary from 0.66 (amphibolites) to 0.65 (garnet-free mafic granulites) to 0.62 (garnetiferous mafic granulites) (Table2). Therefore, the HFS element contents of the studied mafic granulites are considered to have maintained their usual concentrations. This, in turn suggests that the mafic granulites did not undergo partial melting during granulite-facies metamorphism.

To recognize the geochemical alteration of alkali elements during metamorphism, we plot the samples in the (Na_2O+K_2O)% versus Na_2O/K_2O diagram (Supplementary Fig. 4a) of Miyashiro A (1975) and CaO/Al_2O_3–$MgO/10$–$SiO_2/100$ ternary diagram (Supplementary Fig. 4b) of Schweitzer J and Kroner A (1985). All the studied samples fall well within the "unaltered" field, suggesting they maintain the primary igneous geochemistry.

To assess the effect of mobility on HFS elements in the mafic granulites of the present study, we have plotted Zr–Hf, Y–Ho, and Nb–Ta bivariate diagrams (Supplementary Figs. 4c–e). These element pairs display excellent correlations (r^2 up to 0.99) consistent with their relatively limited mobility during metamorphism.

Zr and Hf, Y and Ho, Nb and Ta with identical charges and strikingly similar radii behave nearly identically in most systems on Earth (Mason B and Moore CB, 1982). Therefore, most materials have near chondritic Zr/Hf ratios of about 35–40 (Hoskin PW and Schaltegger U, 2003). However, Zr is preferentially partitioned in zircon over Hf (Claiborne LL et al., 2006). Therefore, moderately high Zr/Hf ratios of the studied amphibolites (50.83) and mafic granulites (garnet free mafic granulite: 49.01; garnetiferous mafic granulite: 33.68) indicate accumulation of zircon (Supplementary Fig. 4c, Table 2).

Y shows greater mobility than Ho during chemical alteration (Babechuk MG et al., 2014). Y/Ho ratios of the primitive mantle and mantle-derived magma are close to 28 (Sun SS and McDonough WF, 1989). Therefore, similar Y/Ho ratios of the studied amphibolite (~28.15) and mafic granulites (garnet-free mafic granulite: 28.97; garnetiferous mafic granulite: 29.33) designate pristine igneous ratios of these elements (Supplementary Fig. 4d, Table 2). Identical Y/Ho ratios in amphibolites and mafic granulites also suggests no partial melting in mafic granulites took place during granulite facies metamorphism.

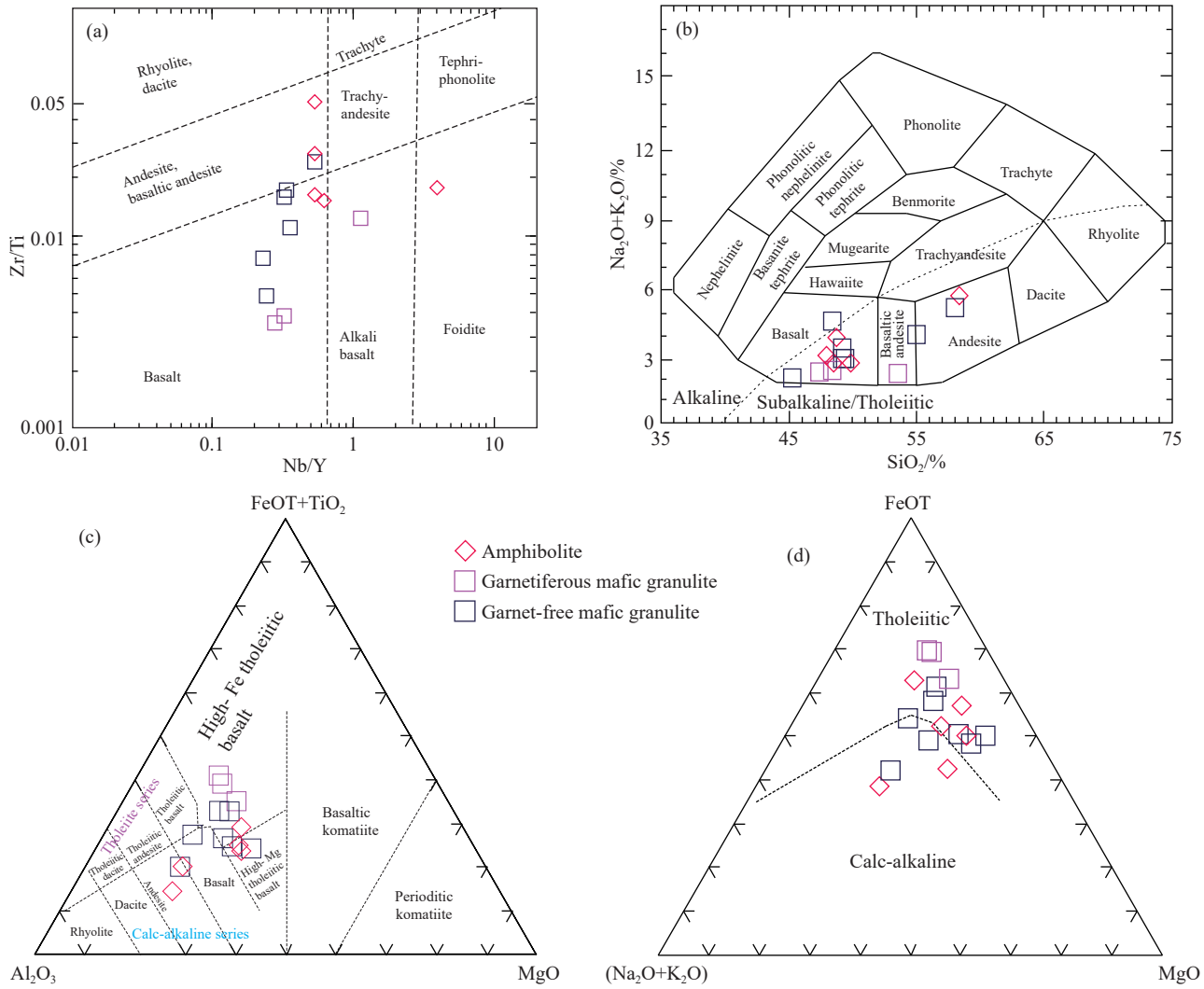

Fig. 4. Classification diagrams: (a) Nb/Y vs. Zr/Ti diagram (after Pearce JA, 1996); (b) SiO_2 vs. Total alkali diagram (after Cox K et al., 1979); (c) (FeO^T+TiO_2)–Al_2O_3–MgO diagram; (d) AFM ternary plot of Irvine TNJ and Baragar WRAF (1971).

Mantle-derived mafic magmas have near-constant Nb/Ta ratios (15–16, Gale A et al., 2013). Amphibolites show high Nb/Ta ratios (av. 28.06), while the mafic granulites of the present study exhibit lower Nb/Ta ratios (ca. 11.16 and 13.96) than those of basalts. Amphibole prefers Nb over Ta (Zhang X et al., 2021). Therefore, high Nb/Ta ratios in amphibolites are related to the abundances of modal amphiboles in the amphibolites. In contrast, the breakdown of amphibole during granulite facies metamorphism of mafic granulites can explain their low Nb/Ta ratios (Table 2; Supplementary Fig. 4e).

5.2. Tectonic Setting of emplacement

On the Th/Yb versus Nb/Yb diagram (Supplementary Fig. 5) of Pearce JA (2008), oceanic basalts (intraplate islands, oceanic plateaus, and plume–distal ocean ridges) plot within the "MORB–OIB'' array, whereas the field of volcanic-arc basalts lies above the array. Subduction-related basalts, alkalic basalts, and crust-contaminated basalts having a good amount of recycled crustal components lie above the MORB–OIB array. Ernst RE (2014) argued that immobile incompatible elements ratios make this diagram transparent to cumulate effects. He recommends further the diagram can also be used for gabbroic rocks with caution. A useful summary of the chemistry of Large Igneous Provinces (LIPs) is demonstrated in the Th/Yb versus Nb/Yb diagram by Ernst RE (2014). Continental LIPs (such as the British Tertiary province and North Atlantic margin province) and Proterozoic dyke swarms (e.g., Mackenzie and Dashigou swarms) plot within and above the mantle array (Supplementary Fig. 5), suggesting a significant contribution of the lithosphere and continental crust. Studied mafic granulites plot both within and above the "mantle array" between the N-MORB and OIB (Supplementary Fig. 5). This suggests mantle-derived magma interacted with the crust or lithosphere.

The tholeiitic character of the studied samples suggests minimal incorporation of the continental crustal component to the mantle source. The transitional elements (Ti and V) remain immobile even in granulite facies (Rollinson HR, 1993). The studied mafic granulites show a high concentration of V (201.62×10^{-6}, 249.17×10^{-6}, and 361.23×10^{-6}), high Ti/V ratios (>20; Fig. 6a), but low La/Nb ratios (Fig. 6b) that are consistent with the geochemical characteristics of flood basalt

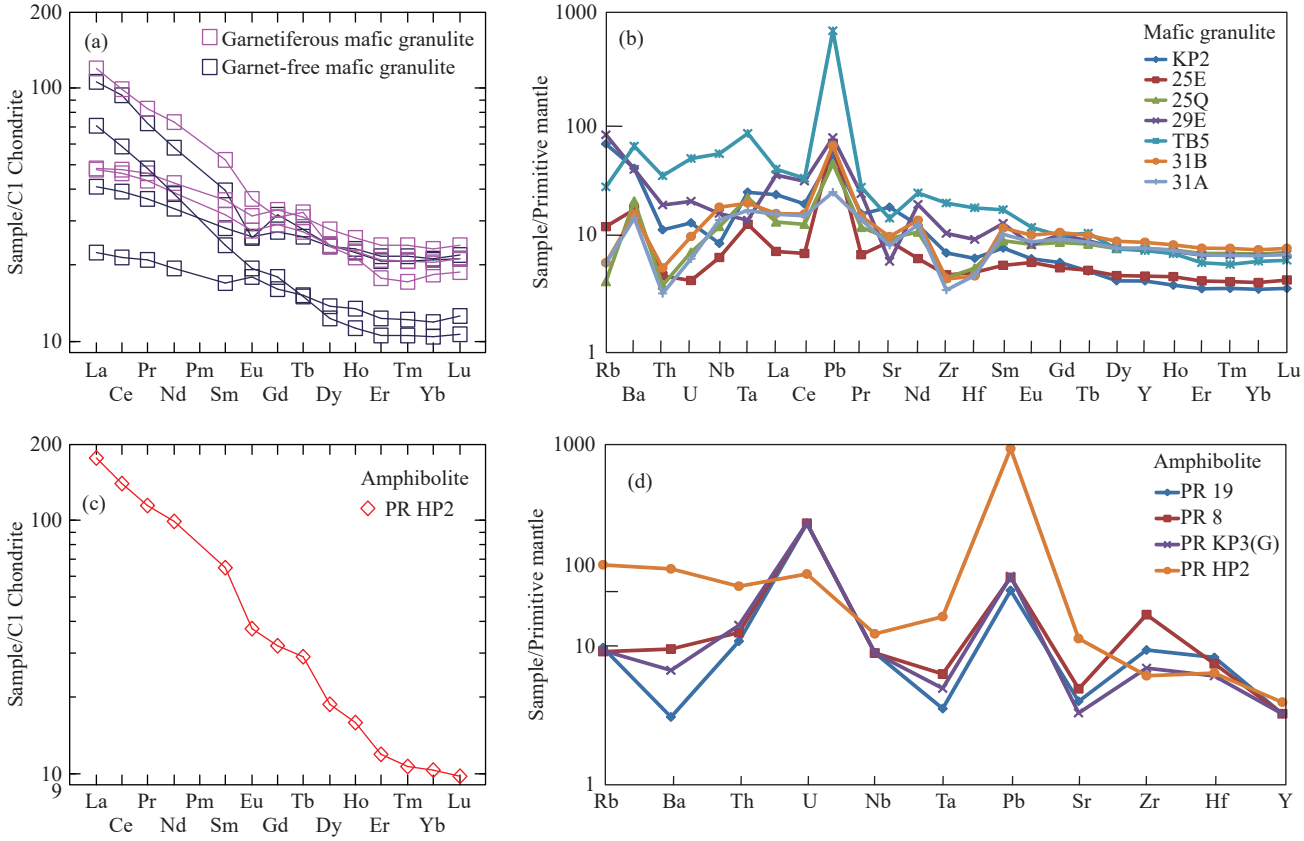

Fig. 5. (a) Chondrite normalized REE diagram of Saltora mafic granulite. Normalization values after McDonough WF and Sun SS (1995). (b) Primitive mantle-normalized spider diagram of Saltora mafic granulite. Normalization values after Sun SS and McDonough WF (1989). (c) Chondrite-normalized REE diagram of Saltora amphibolite. Normalization values after McDonough WF and Sun SS (1995). (d) Primitive mantle-normalized spider diagram of Saltora mafic granulite. Normalization values after Sun SS and McDonough WF (1989).

provinces (Shervais JW, 1982; Erlank AJ et al., 1988). The samples plot predominantly in the MORB and continental flood basalt fields in the V vs. Ti/1000 tectonic discrimination diagram of Shervais JW (1982). However, two rock samples also fall in the ocean island alkali basalt field (Fig. 6a). In the Y vs. La/Nb diagram of Floyd PA et al. (1991), the mafic granulite samples plot in the field of continental flood basalts (Fig. 6b). The studied rocks plot in oceanic subduction unrelated settings and rifted margin-Ocean-Continent Transitional Zone (OCTZ) field in the N-MORB-normalized Th vs Nb discrimination diagram of Saccani E (2015) (Fig. 6c). In the Nb/Sc vs. Sc/Ba discrimination diagram of Han S et al. (2020) the mafic granulites consistently plot within the field of ocean island gabbroic rocks (OIG) (Fig. 6d).

5.3. Physico-chemical condition of metamorphism

The chemical composition of hornblende, garnet, pyroxene, and biotite is widely used by researchers for estimating the temperature, pressure, oxygen fugacity, and water condition of the metamorphic event at which the rocks were metamorphosed.

In the Si (pfu) *vs.* Ti (pfu) diagram (after Xue JZ et al., 1986) of amphiboles, almost all the samples of amphibolites and mafic granulites plot within the metamorphic field. (Supplementary Fig. 6a). In the temperature (°C) vs. pressure (kbar) diagram (Supplementary Fig. 6b), the plots clearly show their granulite facies condition of metamorphism (metamorphic facies divisions are based on the work of Maruyama S et al., 1996). The Ti-in hornblende thermometer was applied for temperature estimation (Otten MT, 1984), and the Al-in hornblende barometer (Schmidt M, 1992) for pressure calculation.

In the Ti vs. (Na+K) (pfu) diagram (after Jin SQ, 1991) and the Al^{vi} vs. Al^{iv} diagram (after Chen G et al., 1988), amphiboles of the investigated samples plot within the granulite facies field. Several plots of amphiboles from Saltora mafic granulite lie within the upper amphibolite facies field, but very close to the granulite facies field (Supplementary Fig. 6c, d).

The garnet-biotite thermometer was used to calculate the peak temperature at which the rocks have formed. Ferry JT and Spear FS (1978) calculated the reactions between garnet and biotite experimentally at a pressure of 0.207 GPa and a temperature range of 500°C–800°C. The Fe-Mg exchange between adjacent garnet and biotite is:

$$Fe_3Al_2Si_3O_{12} + KMg_3AlSi_3O_{10}(OH)_2 \leftrightarrows Mg_3Al_2Si_3O_{12} + KFe_3AlSi_3O_{10}(OH)_2 \quad (1)$$

Some mafic granulites of the present area contain both garnet and biotite. Hence equilibrium constant (K_D) has been obtained using the formula, $K_{D=}{}^{Grt}(X_{Mg}/X_{Fe})/{}^{Bt}(X_{Mg}/X_{Fe})$. Further, Ln K_D = (–2109)/T+0.782, where T denotes the

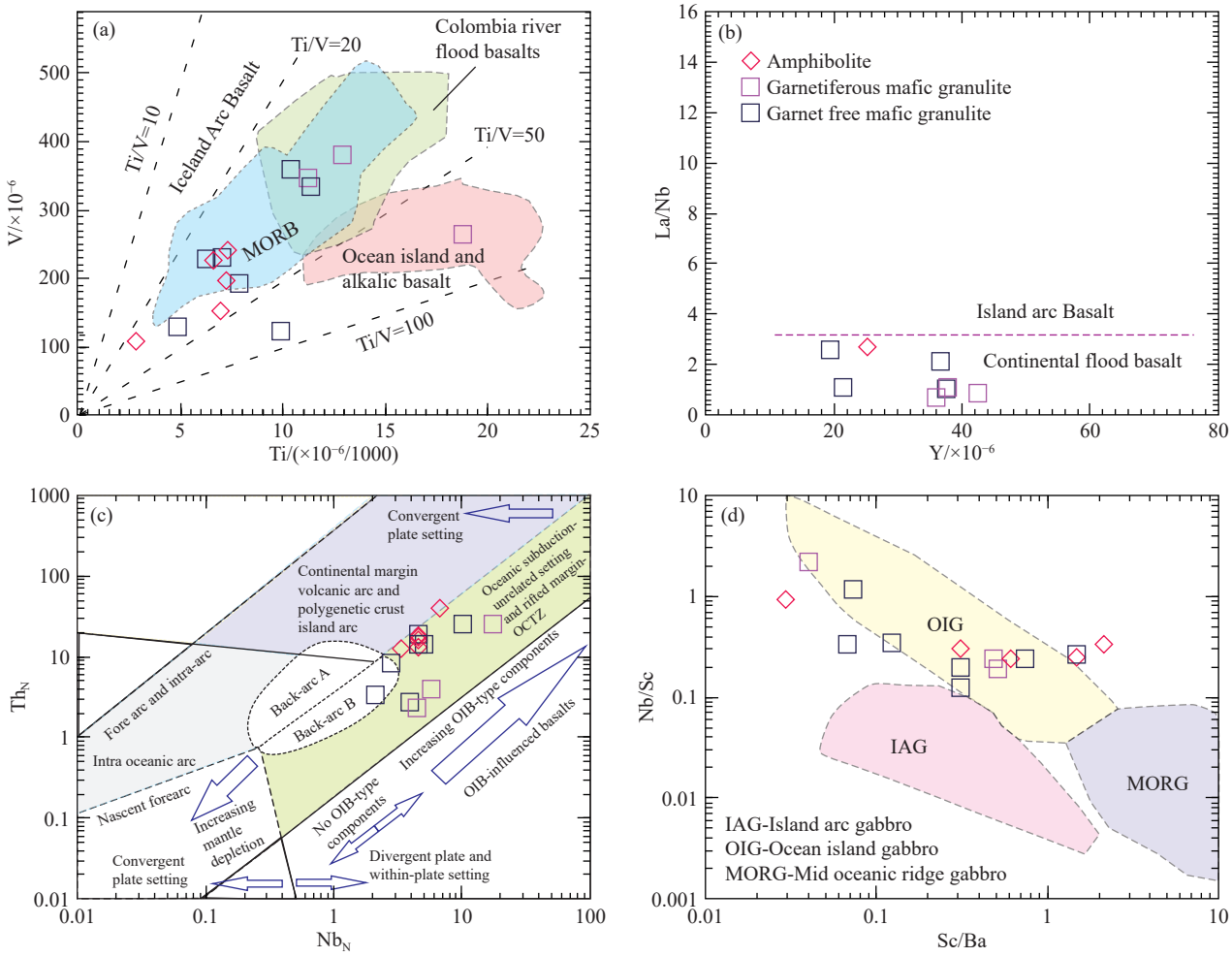

Fig. 6. Plots of amphibolites and mafic granulites in tectonic discrimination diagrams. (a) Ti/1000 *vs.* V diagram of Shervais JW (1982); (b) Y *vs.* La/Nb diagram of Floyd PA et al. (1991); (c) N-MORB-normalized Th *vs.* Nb diagram of Saccani E (2015); (d) Sc/Ba *vs.* Nb/Sc diagram of Han S et al. (2020). Abbreviations: MORB–Mid-oceanic ridge basalt; OIB–Ocean island basalt; OCTZ–Ocean-continent transition zone.

temperature in Kelvin at which the rock was formed.

Using the above formulae, the temperature of metamorphism for Saltora garnetiferous mafic granulite is estimated to be 638.4°C.

Coexisting hornblende and plagioclase are commonly used for thermometric calculations in metaigneous rocks (Blundy JD and Holland TJB, 1990; Holland TJB and Blundy J, 1994). The estimated temperatures at which the rocks have been metamorphosed for amphibolite, garnet-free mafic granulites, and garnetiferous mafic granulites are 780.3°C, 742.9°C, and 726.7°C, respectively. Based on amphibole chemistry with calcic hornblende (Mg#>0.5) (Ridolfi F et al., 2010) the estimated temperatures of amphibolite, garnet-free mafic granulite, and garnetiferous mafic granulite are 910°C, 900.5°C, and 919°C, respectively.

The temperature condition of metamorphism of two-pyroxene mafic granulite has been calculated by coexisting ortho-and clinopyroxene chemistry (Kretz R, 1982; Wells PRA, 1977). Based on pyroxene chemistry, the estimated temperatures for garnet-free mafic granulite are 660.86°C and 797.6°C, respectively (Table 3).

Using the Al-in hornblende barometer by Schmidt M (1992), the amphibolite, garnet-free mafic granulite, and garnetiferous mafic granulite yield the pressure of metamorphism at 610–670 MPa, 650–680 MPa, and840 MPa, respectively. Geobarometry based on net transfer reactions among plagioclase, garnet, biotite, and quartz in the assemblage garnet + plagioclase + biotite + quartz has been calibrated by Hoisch TD (1990) at P = 1.0–11.4 kbar 100–1140 MPa and T = 515–878 °C. Using this calibration, the Saltora garnetiferous mafic granulite yields the pressure of metamorphism of about 850 MPa (Mg end member) and 710 MPa (Fe end member) (Table 3).

The water content can be calculated by the empirical calculation of Ridolfi F et al. (2010) using amphibole chemistry. The average calculated water content of the melt for amphibolite (range: 5.7–6.9%) and garnet-free mafic granulites (range: 5.8%–6.8%) is 6.3% (Table 3).

The oxygen fugacity obtained from amphibole chemistry is (ΔNNO = −0.3) and (ΔNNO = −0.4 to −0.5) respectively for amphibolites and garnet-free mafic granulites (Ridolfi F et al., 2010; Table 3).

We calculate the pressure and temperature conditions during the evolution of the mafic granulites in *P–T* pseudosections with the PERPLE_X software package (see Connolly JAD, 2005; version from August 2011 downloaded

Table 3. Intrinsic parameters of amphibolite and mafic granulite.

Sl No	Rock Type	Sample	Temperature (℃)					
			Hornblende chemistry			Pyroxene chemistry		Garnet-biotite chemistry
			Holland TJB and Blundy J (1994) (edenite + albite = richterite + anorthite)	Otten MT (1984)	Ridolfi F et al. (2010)	Wells PRA (1977)	Kretz R (1982)	Ferry JT and Spear FS (1978)
1	Amphibolite	PR 51	740.2	789.7	897	–	–	–
2		PR 65A	820.4	694.2	923	–	–	–
3	Garnetiferous mafic granulite	PRTB5	726.7	729.4	919	–	–	638.4
4	Garnet-free mafic granulite	PR44	741.6	734.8	883	NA	NA	NA
5		PRKP2	744.2	840.6	918	797.6	660.86	NA

Sl No	Rock Type	Sample	Pressure (MPA)							
			Hornblende barometry						Pl-Gt-Bi-Q barometry	
			Hammarstrom JM and Zen EA (1986)	Hollister LS et al. (1987)	Johnson MC and Rutherford MJ (1989)	Schmidt M (1992)	Link with reference list (edenite + albite = richterite + anorthite)	Ridolfi F et al (2010)	Hoisch TD (1990) (Mg end menber)	Hoisch TD (1990) (Fe end menber)
1	Amphibolite	PR 51	570	600	460	610	619	299	–	–
2		PR 65A	640	680	520	670	690	384	–	–
3	Garnetiferous mafic granulite	PRTB5	820	880	670	840	840	–	850	710
4	Garnet-free mafic granulite	PR44	610	650	490	650	530	344	–	–
5		PRKP2	650	690	630	680	569	377	–	–

Sl No	Rock Type	Sample	Water content (wt.%) and oxygen fugacit		
			Hornblende chemistry		
			Water content of the magma (wt.%)	fO_2 (log unit bar)	ΔNNO
			Ridolfi F et al. (2010)		
1	Amphibolite	PR 51	5.7	−12.3	−0.3
2		PR 65A	6.9	−11.0	−0.3
3	Garnet-free mafic granulite	PR44	6.8	−12.1	−0.4
4		PRKP2	5.8	−12.0	−0.5

from the internet site http://www.perplex.ethz.ch/), along with conventional thermobarometry. For the studied garnetiferous mafic granulite (sample: PR-TB5), the fO_2 is fixed at −15 log units and the water content we consider is 1%. The thermodynamic data sets of Holland TJB and Powell R (2011) were applied for calculations. The following solid-solution models were applied for calculations: cAmph(G): clino-amphibole; Opx(HP): orthopyroxene discovered by Holland TJB and Powell R (1996); Cpx(l): clinopyroxene discovered by Gasparik T (1984, 1985); Gt(HP): garnet discovered by Holland TJB and Powell R (1998); feldspar: both K-feldspar and plagioclase discovered by Fuhrman ML and Lindsley DH (1988); Melt(HP): haIsopleths for Al-in amphibole, An-in plagioclase, Mg# in biotite, clinopyroxene and orthopyroxene, and almandine in garnet have been drawn using the subprogrammes Weremi and Pstable.

The M_1 stage is characterized by the intersection of 0.70 almandine isopleth of garnet and 0.43 Mg# of cpx isopleth. The P-T condition of M_1 is 650 MPa and 770°C (Fig. 7).

The M_2 metamorphic stage is characterized by the intersection of 2.4 isopleths of Al-in amphibole, 2.2 Mg# isopleath of biotite, and 0.56 An in-plagioclase isopleth. The P-T condition of M_2 is 300 MPaand 744°C (Fig. 7).

5.4. Igneous Petrogenesis

Contributions of melts from different sources (e.g., enriched subcontinental lithospheric mantle, asthenospheric mantle etc.) with crustal contamination may explain the geochemical variation of the studied metabasic rocks. We will discuss various models to explain the geochemical variations (e.g., enrichment of LILE and depletion of Ti, Nb, and Ta, etc.), such as (1) differentiation, (2) melt source, and (3) contamination site(s) of the parental magmas of the studied mafic granulites.

5.4.1. Evidence for magmatic differentiation

Both the two types of mafic granulites, garnetiferous and garnet-free, have low MgO (5. 74 and 4.67% respectively) and Ni (57.79×10^{-6} and 43.36×10^{-6} respectively) concentrations. The low abundances of MgO and Ni in these rocks point to extensive fractional crystallization of mafic minerals. The nature of the variation of characteristic

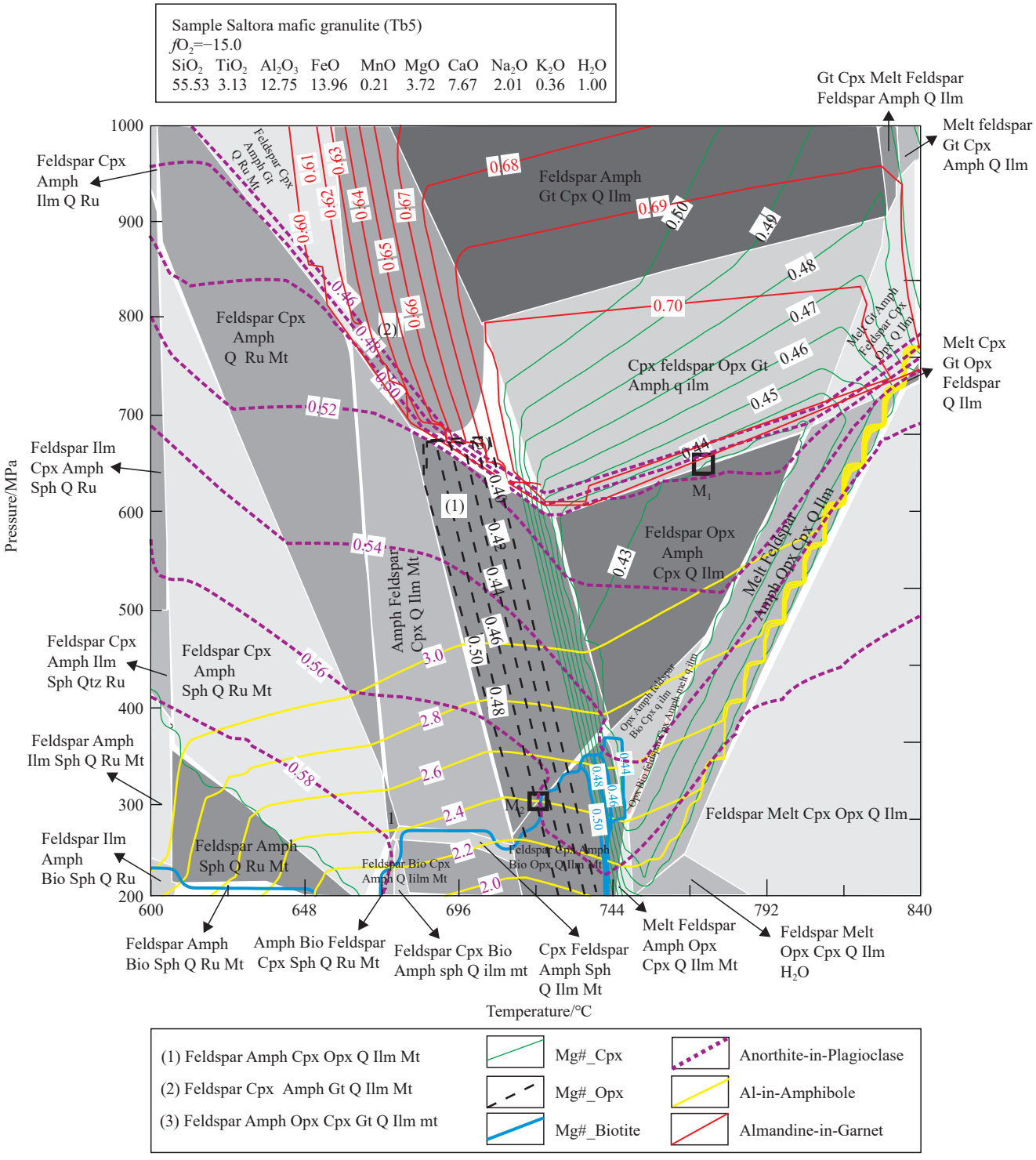

Fig. 7. Temperature (°C) vs. Pressure (MPa) pseudosection of stable mineral assemblages of garnetiferous mafic granulite (PR-TB5) from Saltora area.

geochemical components with SiO_2 (wt.%), as already described (section 3.2.3), suggests a significant role for fractional crystallization of the parent magma.

The chondrite-normalized REE patterns of a melt can be structured either by the amount of partial melting of the source or by crystal fractionation. In basaltic magma, fractionation of olivine, pyroxene, and plagioclase can control the REE-abundances of residual melts (Philpotts A and Ague J, 2009). Olivine fractionation leads to significant enrichment of REE in residual magma without any fractionation among the REE. Plagioclase fractionation also leads to REE enrichment, but with a prominent negative Eu-anomaly in the REE pattern. Augite fractionation results in the enrichment of light REE (La, Ce, and Nd) relative to Sm, while the middle (MREE) and heavy REE (HREE) show a flat pattern. In contrast, orthopyroxene fractionation marks moderate, consistently positively sloped patterns from the Yb to La. Moreover, ratios between strongly incompatible trace

elements will vary considerably, either at very low percentages of partial melting or a high degree of fractional crystallization (Langmuir CH et al., 1992; Klein EM, 2003). Mafic granulites of the present study show both weakly-fractionated REE patterns and moderately LREE-enriched with nearly flat HREE patterns (Fig. 5a).

The moderate relative enrichment of LREE in these rocks could be attributed to clinopyroxene fractionation or a low to moderate percentage of partial melting in the source. Additionally, the absence of significant Eu-anomaly in the Chondite-normalized REE-diagram (Fig. 5a) suggests plagioclase was not a significant fractionating phase.

La/Sm and Th/Hf ratios in basaltic melts increase during partial melting of the source (Allegre CJ and Minster JF, 1978; Martinez-Serrano R et al., 2004; Aldanmaz E, 2002; Aldanmaz E et al., 2008). Increasing Th/Hf ratios with Th of the studied mafic granulites (Supplementary Fig. 7a) and steep trend in a La *vs.* La/Sm diagram (Supplementary Fig. 7b), suggest that partial melting played a significant role in controlling the REE content of these rocks.

5.4.2. Crustal contamination

During ascent, the mafic magmas interact with the continental crust (Currie KL and Williams PR, 1993). Several geochemical plots and ratios can effectively illustrate the commonly marked enrichment in LREE and incompatible elements in continental tholeiites.

A high La/Nb ratio (>1.5) in basaltic rock indicates crustal contamination (Hart WK et al., 1989). The high La/Nb ratios of the Saltora amphibolite (av. La/Nb: 2.69), garnet-free mafic granulite (av. La/Nb: 1.71) and garnet-free mafic granulites (av. La/Nb: 0.88). OIB shows low Zr/Nb ratios (3.2–11.4) and MORB shows high Zr/Nb ratios (30). The low Zr/Nb ratios of Saltora amphibolite (av. Zr/Nb: 15.05), garnetiferous mafic granulites (av. Zr/Nb: 11.04) and garnet-free mafic granulites (av. Zr/Nb: 4.40 indicate similarity with OIB (Table 2; Supplementary Fig. 8a).

Luttinen AV (2018) recently introduced the ΔNb parameter for quantifying the abundance of Nb relative to Zr and Y.

$$\Delta Nb = 1.74 + \log(Nb/Y) - 1.92 \times \log(Zr/Y) \quad (2)$$

OIB and other oceanic basalts related to mantle-plume, commonly show high-Nb (Nb-undepleted) compositions. In contrast, normal-MORB displays the low-Nb (Nb-depleted) values. The Nb values of basalts are feebly affected by the degrees of mantle melting. Prolonged fractionation of calcic pyroxene in evolved magma slightly decreases the ΔNb values in the derivative magma. In a continental setting, crustal contamination or assimilation of SCLM material can reduce the Nb values of basalts (Luttinen AV, 2018). Luttinen AV (2018) proposed ΔNb vs. La/Nb and ΔNb vs. Th/Nb diagrams to evaluate the degree of crustal contamination, wherein he defined the field of crustal contamination. All the studied samples plot outside the field of crustal contamination (Table 2; Supplementary Fig. 8b).

5.4.3. Enrichment of the source mantle

Mantle metasomatized by subducting crust-derived fluid will produce magmas having high Ba/Th (>170) ratio (Hawkesworth CJ et al., 1997) and high Pb/Ce (>0.1) ratio (Elburg MA et al., 2002). The Ba/Th ratio is high (av. 46.89 in amphibolite, av. 194.88 in garnet-free mafic granulite, and av. 258.71 in garnetiferous mafic granulite) in the studied samples, suggesting fluid-derived metasomatism of the source mantle. The Pb/Ce ratio is high, both in amphibolite (av. 0.37) and garnet-free mafic granulite (av. 0.18) and garnetiferous mafic granulite (av. 0.34). The high Ba/La and low Th/Nd ratios in the studied mafic granulites suggest slab-derived fluids metasomatized the mantle source (Table 2; Fig. 8a).

The La/Nb and La/Ba ratios remain unchanged during partial melting or fractional crystallization and effectively indicate mantle-source (Ernst RE, 2014). Three garnetiferous mafic granulite samples of Saltora plot within the OIB field on La/Nb and La/Ba diagrams (Fig. 8b). Another three samples of garnet-free mafic granulites and one amphibolite plot within the field of Karoo dolerite (Fig. 8b). The high La/Nb ratio (>1) and low La/Ba ratio (<0.1) of these rocks suggest the parental magma originated from the partial melting of the lithospheric mantle (cf., Jourdan F et al., 2009).

According to La Flèche MR et al. (1998), lower Ta/La and Hf/Sm ratios in the mafic magma compared to the depleted mantle, together with high-μ mantle values, indicate carbonate metasomatism at the source. The studied samples mostly plot close to the fields of mantle source metasomatized by carbonate in the $(Ta/La)_N$ vs. $(Hf/Sm)_N$ diagram (after La Flèche MR et al., 1998) (Fig. 8c).

In summary, the studied mafic granulites are derived from a metasomatized mantle. The mantle metasomatism took place by subducting crust-derived fluid.

Very recently, Pearce JA et al. (2021) have shown that intraplate, plume-derived magmas exhibit one of the following three arrays when plotted on the Th/Nb vs. TiO_2/Yb diagram (Fig. 8d): Type I: MORB-OIB-OPB (plume) array (where OPB = oceanic plateau basalt); Type II: subduction-modified lithospheric mantle (SZLM) array; and Type III: a combination of the first two arrays. Furthermore, they show three sub-types of Type-III. Type IIIa extends from the SZLM to the MORB-OPB part of the array, whereas Type IIIb extends from the SZLM to the OIB-OPB part of the array, and Type IIIab extends from the SZLM to the small transitional MORB-OIB-OPB field. The mafic granulite samples of the study follow the IIIab trend on the Th/Nb vs. TiO_2/Yb diagram of Pearce JA et al. (2021) (Fig. 8d). According to Pearce JA et al. (2021), basalts following the Type-IIIab trend represent interactions between plume-sourced and SZLM-sourced magmatic end-members.

5.4.4. Mantle mineralogy and melting processes

Melts derived from the asthenospheric mantle exhibit high

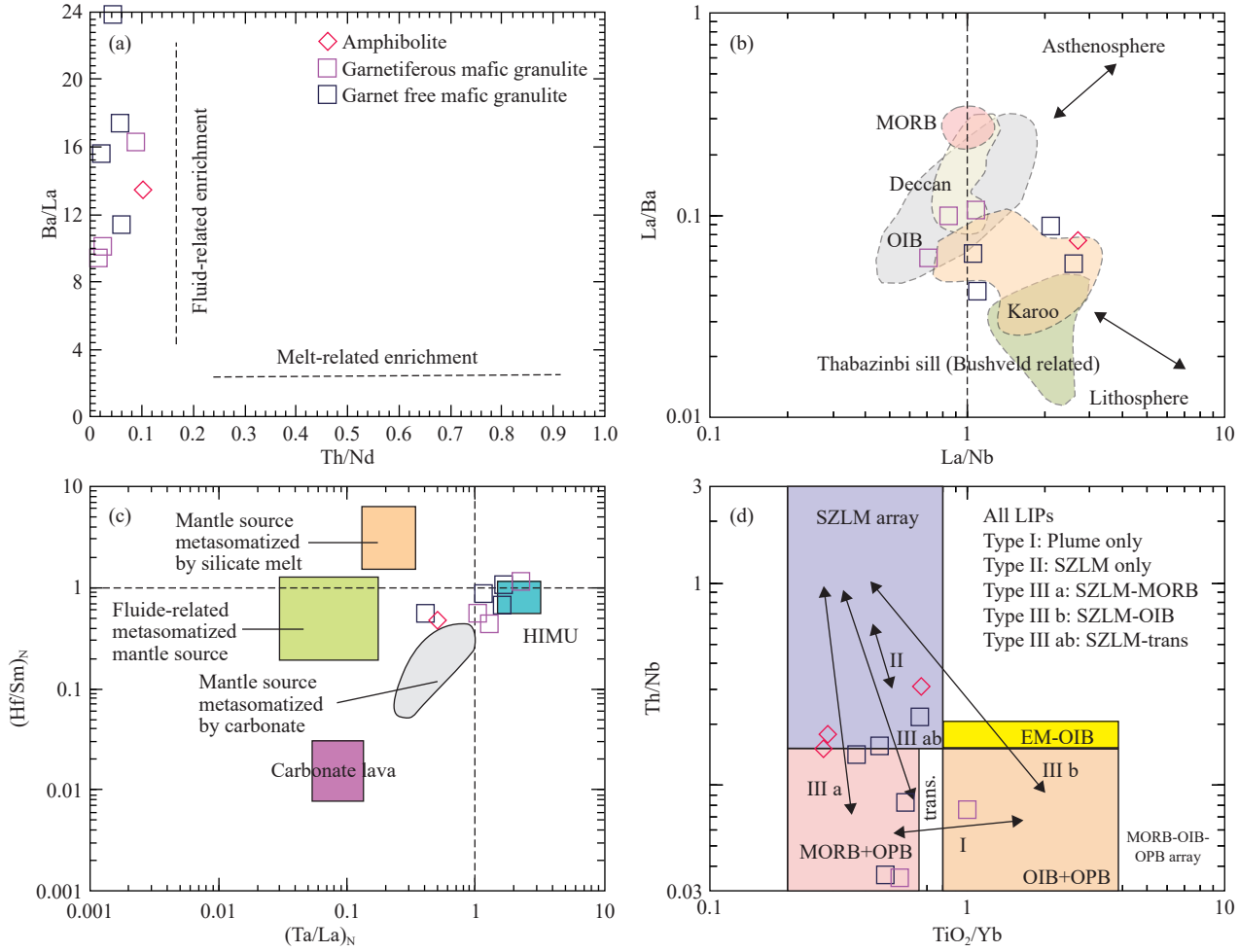

Fig. 8. Plots of trace element ratios of amphibolites and mafic granulites of Saltora in various diagrams. (a) Th/Nd vs. Ba/La diagram showing subducted slab-derived fluid and melt-derived enrichment trends. (b) La/Nb vs. La/Ba diagram. Fields of Thabazinbi sill, Karoo dolerite, OIB (Ocean Island basalt), Deccan basalt and MORB (Mid-oceanic ridge basalt) are after Ernst RE (2014). (c) (Ta/La) vs. (Hf/Sm) diagram after La Flèche MR et al. (1998). Normalization values of primitive mantle after Sun SS and McDonough WF (1989). (d) TiO_2/Yb vs. Th/Nb diagram of Pearce JA et al. (2021) showing principal types of LIP basalt dispersion. Type I: plume array; Type II: SZLM array; and Type III: plume-SZLM interactions. Type IIIa: MORB+OPB-SZLM interractions; Type IIIb: OIB+OPB-SZLM interractionsi; Type IIIab: SZLM-MORB+OPB+OIB interractions. HIMU–High-μ mantle; SZLM–subduction-modified lithospheric mantle; EM–Enriched Mantle; OIB–Ocean Island basalt; OPB–Oceanic plateau basalt.

Nb/La ratios, ranging from 1.3 (OIB and E-MORB) to 0.9 (N-MORB) (Sun SS and McDonough WF 1989; Smith EI et al., 1999). In contrast, the SCLM-derived melts show low Nb/La ratios and are equivalent to that of the continental crust (CC=0.4; Wang L. et al., 2014). The Saltora amphibolite and mafic granulites show low to high Nb/La ratios (av. 0.37 in amphibolite, av. 0.68 in garnet-free mafic granulite, and av. 1.17 in garnetiferous mafic granulite), which suggests their origin from a mixed lithospheric-asthenospheric mantle source (Table 2; Fig. 9a; see also Condie KC, 1997).

If garnet remains as a residue during melting, the parental melt would have a depleted HREE character, with Y/Yb ratios >10 and primitive-mantle normalized $(Ho/Yb)_N$ ratios >1.2. A moderate range of Y/Yb ratios characterizes the amphibolite (av. 6.12), garnet-free mafic granulites (10.93) and garnetiferous mafic granulites (av. 10.99) of Saltora area. Additionally, the moderate $(Ho/Yb)_N$ ratios are characteristics of both the amphibolite, garnet-free mafic granulites, and garnetiferous mafic granulites (1.53, 1.09, and 1.13, respectively). The moderate Y/Yb and $(Ho/Yb)_N$ ratios indicate that spinel and minor garnet were present as a residual phase in the source mantle. The low $(Tb/Yb)_N$ ratios (2) in the basaltic rocks also suggest the parental magmas were derived from a spinel-bearing peridotite source (Xu YG, 2001; Wang P et al., 2002). The disposition of the studied samples in the primitive-mantle-normalized $(La/Sm)_N$ vs. $(Tb/Yb)_N$ diagram (Fig. 9b) suggests their origin from a transitional spinel-bearing source.

Giuseppe P Di et al. (2018) modeled the partial melting of spinel and garnet peridotite mantle sources. According to this model (Dy/Yb vs. Yb diagram, Fig. 9c), 5% to 10% melting of a spinel peridotite can yield the parental magma of the garnetiferous mafic granulites. However, the parental magma of the garnet-free mafic granulites can be produced by 7% to 20% partial melting of spinel peridotite (Fig. 9c).

Brandl PA et al. (2015) compiled literature data from melting experiments of dry peridotite and carbonated peridotite. These authors plot the melt composition and the

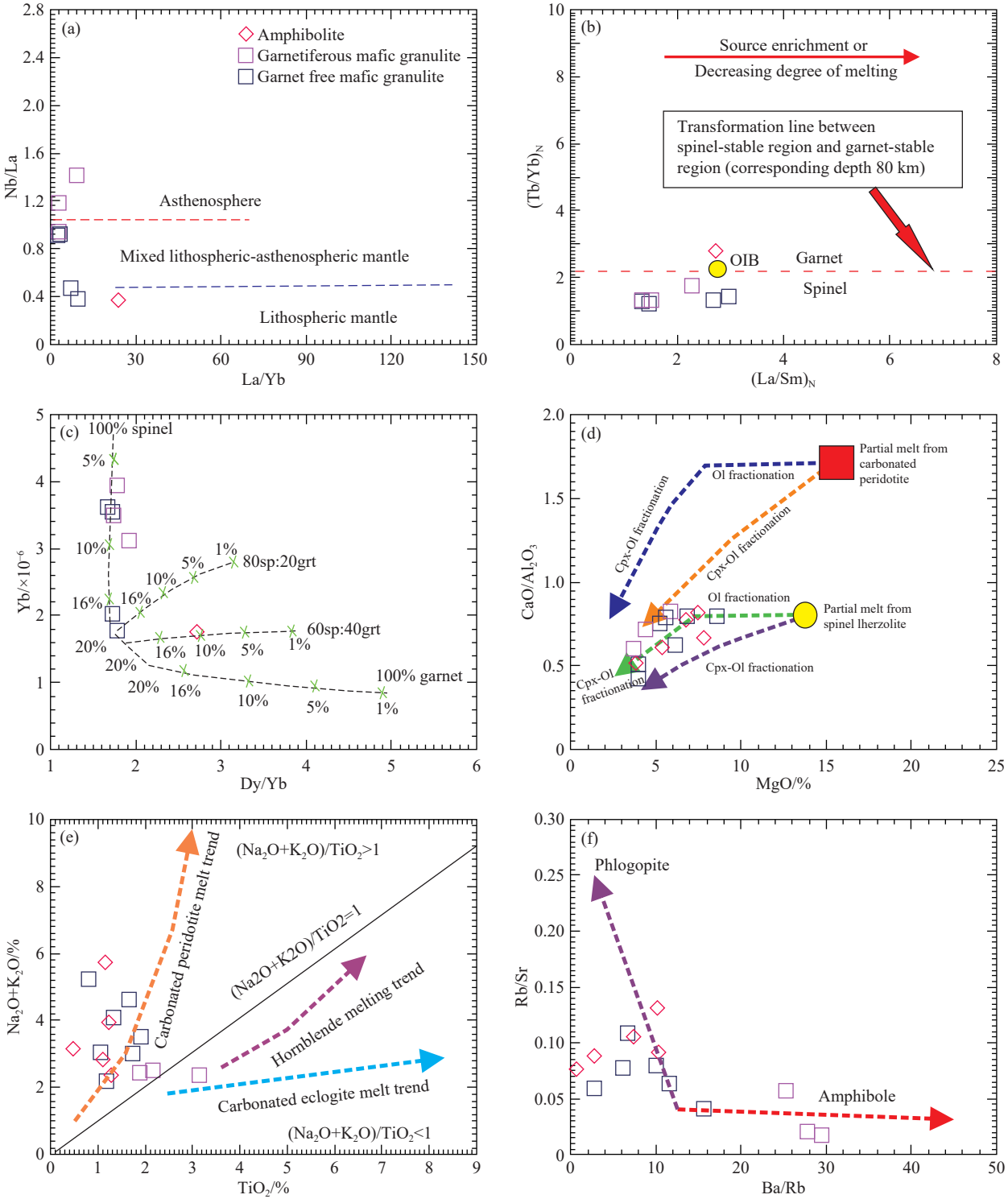

Fig. 9. Plots of amphibolites and mafic granulites in discrimination diagrams to identify the source mantle. (a) La/Yb vs. Nb/La diagram (after, Abdel-Rahman AFM and Nassar PE, 2004). (b) $(La/Sm)_N$ vs. $(Tb/Yb)_N$ diagram (normalized to primitive mantle values of Sun SS and McDonough WF, 1989). The boundary between products of spinel- and garnet-dominated melting is from Wang P et al. (2002) and references therein; OIB from Sun SS and McDonough WF (1989). (c) Dy/Yb vs. Yb diagram. Partial melting lines are drawn by Giuseppe PDi et al. (2018) for garnet and spinel-bearing lherzolite sources. (d) MgO (wt %) vs. CaO/Al_2O_3 diagram of Brandl PA et al. (2015). (e) TiO_2 vs. (Na_2O+K_2O) diagram of Zeng G et al. (2010). (f) Ba/Rb vs. Rb/Sr diagram of Furman T and Graham D (1999) showing controls of phlogopite and amphibole of mantle source. Sp–spinel; Gt–garnet; Ol–olivine; Cpx–clinopyroxene.

liquid line of descent on fractionation of olivine and olivine+pyroxene generated by melting spinel lherzolite (KLB-1) at 1.5 GPa and 1350°C (Hirose K and Kushiro I, 1993) on a MgO (wt.%) vs. CaO/Al_2O_3 diagram (Fig. 9d). They have also plotted the fractionation trend of primary melt produced by a carbonated peridotite melting with 1.0 % CO_2 (PERC-3) at 3.0 GPa and 1350°C (Dasgupta R et al., 2007) on the same diagram (Fig. 9d). The parental magma of mafic

granulite samples was formed through olivine fractionation, followed by clinopyroxene+olivine fractionation from the partial melt derived from natural spinel-lherzolite. Alternately, extreme fractionation of olivine and clinopyroxene originating from the partial melting of a carbonated peridotite melt can give rise to the parental magma of the investigated samples.

Zeng G et al. (2010) have plotted melting trends of carbonated peridotite melt trend, hornblende melt trend, and carbonated eclogite melt trend in a TiO_2 vs. (Na_2O+K_2O) diagram (Fig. 9e). The studied metamafics have (Na_2O+K_2O)/TiO_2>1 and clearly follow the melting trend of carbonated peridotite mantle (Fig. 9e).

The Cenozoic basalts of east China show high CaO/Al_2O_3 ratios (>0.6) and superchondritic Zr/Hf ratios (>44), as well as negative Zr (Zr/Zr*=0.54), Hf (Hf/Hf*=0.57), and Sr (Sr/Sr*= 0.73) anomalies in a primitive mantle-normalized spider diagram (Zeng G et al., 2010). According to Zeng G et al. (2010), the Cenozoic basalts of east China were formed from the melting of a carbonated peridotite mantle. The metamafic rocks in this study have high CaO/Al_2O ratios (avg. 0.68). Moreover, the studied metamafics show prominent negative Zr, Hf, and Sr anomalies in the primitive-mantle normalized spider diagram (Fig. 5b, d). The Saltora metamafics have an average Zr/Hf ratio of 46.37 (Table 3), higher than the chondritic Zr/Hf ratio of 44. All these geochemical characteristics are similar to those of the Cenozoic basalts of east China, which were emplaced in an intracontinental rift setting. Therefore, based on the significant geochemical similarities between the Cenozoic basalts of east China and the metamafics of Saltora, a carbonated peridotite mantle can also be inferred as the source for the metamafics of this study.

The studied amphibolite and garnet-free mafic granulite rocks have low Rb/Sr ratios (0.09 and 0.11) but high Ba/Rb ratios (6.52 and 14.76), indicating the predominance of phlogopite in the source mantle. However, low Rb/Sr (0.03) and high Ba/Rb (27.52) in garnetiferous mafic granulite indicate amphibole in the source mantle (Fig. 9f).

Therefore, in summary, the trace-element characteristics of these rocks indicate source mantle for the magma was a metasomatized (carbonated) amphibole-spinel-garnet peridotite of mixed asthenosphere-lithosphere.

5.5. Regional correlation and Tectonic evolution

The Grenville orogeny took place between 1.3 Ga and 1.1 Ga and involved collisions associated with the formation of the supercontinent Rodinia (Li ZX et al., 2008). Global, intracontinental magmatic events occurred at around 1100–1000 Ma. For example, voluminous mafic and granitic magma was emplaced in the Ngaanyatjarra Rift of central Australia between 1075 Ma and 1026 Ma (Evins PM et al., 2010). The mafic dyke swarms intruded the basement rocks of Bahia State, eastern Brazil during post-assembly extension in the Rodinia Supercontinent at around 1000 Ma (Correa-Gomes LC and Oliveira EP 2000). Voluminous mafic magmatism in the diabase province of southwestern USA occurred between 1140 and 1040 Ma (Bright RM et al., 2014). The Mid-Continental Rift of North America records a major rifting and associated magmatism at ca. 1100 Ma (Hanson RE et al., 2004; Stein S et al., 2018). Dolerite dykes in Laanila and Kautokeino, are examples of intracontinental magmatic events at around 1100 Ma in the northern Fennoscandian shield (Mertanen S et al., 1996).

In the preceding sections, we have shown that the mafic dykes of Saltora originated from a carbonated peridotite mantle and were emplaced in an intracontinental rift setting. For regional correlation we summarize here the geochemical characteristics of mafic dyke swarms of the Saltora belonging to the CGC of the present area, mafic dykes of Dhanbad, adjacent Dhanbad district, India (Kumar A and Ahmad T, 2007), Alcurra dolerite dyke suite, Ngaanyatjarra Rift, west Musgrave Province, Central Australia (Wingate MT et al., 2004; Howard HM et al., 2009; Evins PM et al., 2010), and the dykes of the Mahoba, Bundelkhand craton, India (Choudhary BR et al., 2019; Pradhan VR et al., 2012) based on published geochemical data in Table 4.

Despite their wide separation, the mafic rocks of the Saltora and Dhanbad in the CGC terrain, and Mahoba dykes from the adjacent Bundelkhand craton and Alcurra dolerite dyke suite, Ngaanyatjarra rift, west Musgrave Province, Central Australia, show remarkably similar mid-oceanic ridge basalt–normalized trace element patterns (Fig. 10). Mafic rocks from the Saltora and the Alcurra dolerite dyke suite show enrichment in large ion lithophile elements (LILEs) relative to high field strength elements (HFSEs) and positive Pb anomalies in MORB–normalized spider diagrams (Fig. 10). These mafic rocks have a $(La/Yb)_{CN}$ of around 5, and a $(Gd/Yb)_{CN}$ of 1–2 (CN is chondrite normalized). Table 4 shows that all these mafic rocks exhibit a tholeiitic differentiation trend, a low SiO_2 content, and a low Mg# (50). Melting of a subduction-modified lithospheric mantle is suggested for the magma genesis of all these occurrences.

The Alcurra dolerite dyke suite (1067±8 Ma) was emplaced in the intercontinental Ngaanyatjarra Rift (1085–1040 Ma; Wingate MT et al., 2004; Howard HM et al., 2009). The Ngaanyatjarra Rift was initiated after Musgrave orogeny (1220–1150 Ma; Aitken AR et al., 2013). The Dashigou LIP of the North China Craton (925 Ma) is proposed to be correlatable with the Bahia-Gangila LIP of the São Francisco-Congo Craton (Su X et al., 2021). Kumar A and Ahmad T (2007) proposed that the Dhanbad area's (within the CGC) amphibolite dykes were emplaced in a continental rift. Kumar D et al. (2022) have shown that the amphibolite dykes from western parts of the CGC were emplaced in a post-collisional intra-continental extensional tectonic setting at around 950 Ma.

The present study has shown that the parental magma of the mafic dykes from Saltora areas was derived from the mixed asthenosphere-subcontinental lithospheric mantle. The subcontinental lithospheric mantle was metasomatized by subduction-related fluids and carbonatite melts. Both the post-collisional and plume-related models are consistent with such

Table 4. Compositional characteristics and related aspects of mafic dykes from Saltora of CGC and other regions.

Area	Saltora garnet-free mafic granulites	Saltora garnetiferous mafic granulites	Saltora amphibolite	Dhanbad within the CGC	Mahoba, Bundelkhand craton, India	Warakurna, Western Australia
SiO_2 (wt.%)	45.32–58.02	47.35–53.53	47.97–58.31	46.65–51.87	51.09–52.34	48.3–54.6
Mg#	45.16–62.33	35.59–46.10	54.38–63.82	46–73	42.50–45.68	50–73.5
LILE	Enriched	Enriched	Enriched	Enriched	Enriched	Enriched
HFSE	Depleted	Depleted	Depleted	Depleted	Depleted	Depleted
Pb anomaly	Strong positive	Strong positive	Strong positive	No data	Strong positive	Strong positive
Nb anomaly	No anomaly	No anomaly	No anomaly	Negative	Negative	Negative
LREE	Fractionated	Fractionated	Fractionated	Fractionated	Fractionated	Fractionated
HREE	Nearly flat	Nearly flat	Nearly flat	Nearly flat	Nearly flat	Nearly flat
Magma series	Tholeiitic	Tholeiitic	Tholeiitic	Tholeiitic	Tholeiitic	Tholeiitic
Tectonic setting	Within plate	Within plate	Within plate	Within plate	Within plate	Within plate
Source	Interactions between lithospheric and asthenospheric (spinel peridotite) mantle sources	Interactions between lithospheric and asthenospheric (spinel peridotite) mantle sources	Interactions between lithospheric and asthenospheric (spinel peridotite) mantle sources	Enriched mantle	Spinel lherzolite mantle, contaminated by metasomatised lithospheric mantle	Subduction modified lithospheric mantle
Age	Grenvillian	Grenvillian	Grenvillian	Mesoproterozoic	1096 ± 19 Ma	Ca. 1070 Ma
Reference	This study	This study	This study	Kumar and Ahmad (2007)	Choudhary et al. (2019); Pradhan et al. (2012)	Wingate et al. (2004)

a magma source.

If the studied Saltora dykes are plume-related, it would be difficult to explain why these are restricted within the CGC and why similar dyke swarms are not recorded from the other areas of the north Indian cratonic block. Several authors, however, proposed a Grenvillian collisional event between the north and south Indian blocks in the CGC (and along the Central Indian Tectonic Zone, CITZ) at 1000–950 Ma (see Section 2, Geological setting). In the early stages of this collision, the collapse of the upper and middle crust took place. Rapid decompression produced internal heating, which induced partial melting of the middle crust and created a large volume of felsic magma to form the migmatitic country of the CGC (c. 1178 Ma, cf. Ray Barman T et al., 1994; Goswami B and Bhattacharyya C, 2010). The migmatites were folded during the succeeding deformation. In line with this proposition, we suggest that the studied dyke swarms in the CGC were emplaced in a post-collisional environment. After the Grenvillian collisional-related deformation, the thickened crust in the CGC became gravitationally unstable and generated fractures for the emplacement of the mafic dykes. Based on the remarkable geochemical similarity between the metamafics of Saltora in the CGC and the 1067±8 Ma Alcurra dolerite dykes of the Ngaanyatjarra Rift in Musgrave province, we propose a similar emplacement age for the Saltora metamafics. Porphyritic granitoids with megacrysts of K-feldspar have emplaced in the CGC between 1059 Ma and 1065 Ma (Singh Y, 1992; Singh Y and Krishna V, 2009). After the emplacement of the mafic dykes in the Saltora area, orthopyroxene-bearing porphyritic granites were emplaced just outside of the western margin of the study area at around 1071 Ma (Ray Barman T et al., 1994). Goswami B and Bhattacharyya C (2014) described mingling and hybridization between coeval mafic magma and the c. 1071 Ma porphyritic granites. The porphyritic granite magma and the coeval mafic magmas were emplaced along the fractures of the North Purulia Shear Zone (Goswami B and Bhattacharyya C, 2014; Das S et al., 2020). Porphyritic granites with coeval mingled gabbros are also recorded in the Ngaanyatjarra Rift between 1058 Ma and 1063 Ma (Evins PM et al., 2010). Based on the notable similarity between texture (porphyritic with K-feldspar megacrysts), characteristic coeval mafic magmatism, and similar emplacement age, a tentative correlation between the porphyritic granites of the CGC and those of the Ngaanyatjarra Rift is proposed.

During intracontinental rifting, the upwelling of the asthenospheric mantle supplied extra heat to the overlying Subcontinental Lithospheric Mantle (SCLM), causing partial melting of the SCLM (Supplementary Fig. 9). The SCLM was previously metasomatized by subduction-related fluids. The mixing of asthenosphere and SCLM-derived magma produced large amounts of mafic magma. At this stage, several extensional fractures are likely to develop parallel to the orogen (nearly E-W trend) the mafic magmas were emplaced in the Saltora area via post-collisional extensional fractures along the E-W trend. The North Purulia Shear Zone (NPSZ; Fig. 1b, c) is interpreted as a fossil post-collisional extensional fracture (Supplementary Fig. 9). Mafic magmas emplaced

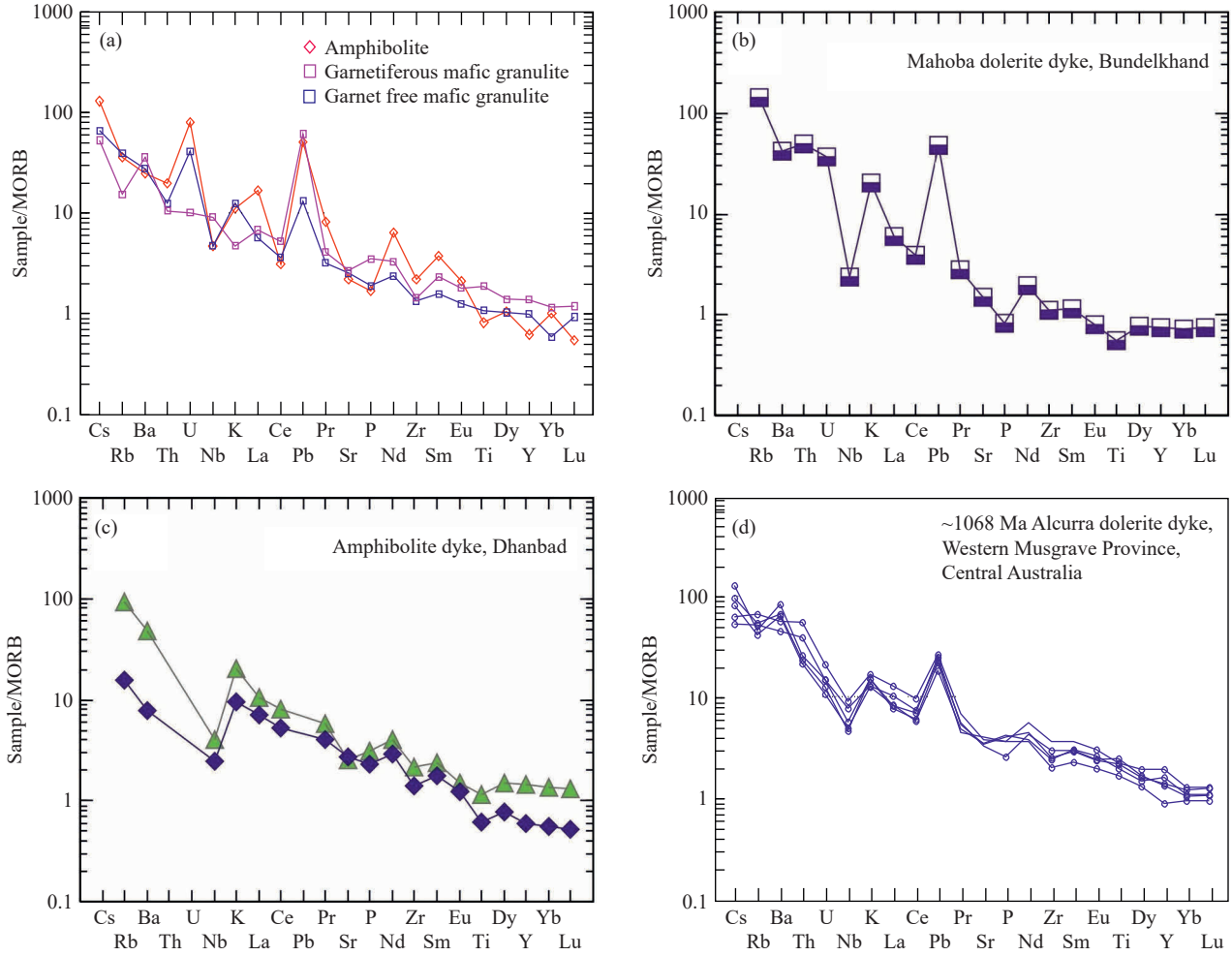

Fig. 10. Spider diagrams for the (a) average of amphibolite and mafic granulite dykes of Saltora (b) Mahoba dolerite dykes, Bundelkhand; (c) Type-1 and Type-3 amphibolite dykes of Dhanbad (data from Kumar A and Ahmad T, 2007); (d) range and average composition of mafic sills, dykes and basalts of Warakurna large igneous province, Australia (data from Wingate MT et al., 2004). MORB (mid-ocean-ridge basalt) normalization values after Sun SS and McDonough WF (1989).

through the fracture of the NPSZ (Supplementary Fig. 9). Post-collisional felsic intrusions in the CGC are widespread (Goswami B and Bhattacharyya C, 2014; Goswami B et al., 2018; Basak A et al., 2019; Das S et al., 2020; Roy P et al., 2020; Sequeira N et al., 2020). These granite bodies were emplaced at about 1000 Ma along the North Purulia Shear Zone (NPSZ).

6. Conclusions

Based on the field, petrological, and geochemical studies of the metamorphosed mafic rocks in the Saltora area of the Chhotanagpur Gneissic Complex, eastern Indian craton, the following conclusions have been drawn:

(i) The Grenvillian, brown hornblende amphibolite, and mafic granulite dykes of Saltora, the Chhotanagpur Gneissic Complex (CGC), were emplaced in an intraplate rift. The rocks were metamorphosed under granulite facies conditions in two stages during D_3-deformation. Pseudosection modelling reveals that the M_1 metamorphism happened at 6.5 kbar and 770°C, while the M_2 metamorphism followed at about 3.0 kbar and 744°C.

(ii) The metamafics are enriched in LILE, depleted in HFSE, display strong fractionation of LREE, nearly flat HREE patterns in a chondrite-normalized REE diagram, and show a tholeiitic differentiation trend. Their parental magma was derived from a carbonated peridotite mantle. Slab-derived fluid and carbonatite melt metasomatized the subcontinental metasomatized mantle (SCLM) in a previous subduction. The parental magma of the garnet-free mafic granulite variety can be generated by about 7%–10% partial melting of the spinel-peridotite mantle (SCLM).

(iii) The metamafic dykes of Saltora were emplaced during crustal extension in the post-collisional tectonic setting, possibly around 1070 Ma. The remarkable geochemical similarity between the mafic dykes of Saltora and Dhanbad, the ca. 1096 Ma Mahoba (Bundelkhand craton), and the ca. 1070 Ma Alcurra mafic dykes in Australia supports a genetic link.

CRediT authorship contribution statement

Bapi Goswami conceived the presented idea. Poulami Roy carried out the fieldwork and experiments. All authors discussed the results and contributed to the final manuscript.

Declaration of competing interests

The authors declare no conflicts of interest.

Acknowledgements

This study was funded by a major research project grant from the UGC (F.-43-367/2014(SR)) and teachers' research grant from the University of Calcutta awarded to Dr Bapi Goswami. DST-sponsored Women Scientist scheme-A (SR/WOS-A/EA-47/2018 (G) dated 06.05.2019) awarded to Ms. Poulami Roy is highly acknowledged for their financial help. We thank Prof. Arijit Roy, Prof. Gautam Ghosh and Mr Sujit Kumar Bhaduri, Presidency University, Kolkata, and Dr Manoj Jaiswal and Mr Biswajit Giri, Indian Institute of Science, Education and Research (IISER), Kolkata, West Bengal for arranging major- and trace-element analyses. We are also very grateful to Prof. Manikyamba, Dr Ram Mohan, Dr Satyanarayanan and Mr D Linga for analysis of trace elements including REE at the National Geophysical Research Institute (NGRI), Hyderabad, India. Thanks are due to Ms. Arya Ghosh, Ms. Shampa Khan and Ms. Susmita Mandal (EPMA Laboratory, CHQ, Geological Survey of India, Kolkata) for providing Electron Microprobe facilities. We convey our sincere gratitude to the two anonymous reviewers for their constructive suggestions.

Supplementary dataset

Supplementary Figures 1–9 and Supplementary Tables 1–10 of this article can be found online at doi: 10.31035/cg20220082.

References

Abdel-Rahman AFM, Nassar PE. 2004. Cenozoic volcanism in the Middle East: Petrogenesis of alkali basalts from northern Lebanon. Geological Magazine, 141(5), 545–563. doi: 10.1017/S0016756804009604.

Acharya A, Ray S, Jana P. 2005. Integrated mineral search in the eastern sector of North Purulia Shear Zone (NPSZ) between Raghunathpur and Santuri-Saltora (P-II). Record, Geological Survey of India, 136(3), 61–64.

Acharyya SK. 2003. The nature of Mesoproterozoic Central Indian Tectonic Zone with exhumed and reworked older granulites. Gondwana Research, 6, 197–214. doi: 10.1016/S1342-937X(05)70970-9.

Ague JJ. 2017. Element mobility during regional metamorphism in crustal and subduction zone environments with a focus on the rare earth elements (REE). American Mineralogist:Journal of Earth and Planetary Materials, 102(9), 1796–1821. doi: 10.2138/am-2017-6130.

Aitken AR, Smithies RH, Dentith MC, Joly A, Evans S, Howard HM. 2013. Magmatism-dominated intracontinental rifting in the Mesoproterozoic: The Ngaanyatjarra Rift, central Australia. Gondwana Research, 24(3–4), 886–901. doi: 10.1016/j.gr.2012.10.003.

Aldanmaz E, Yaliniz MK, Guctekin A, Goncuoglu MC. 2008. Geochemical characteristics of mafic lavas from the Neotethyanophiolites in western Turkey: implications for heterogeneous source contribution during variable stages of ocean crust generation. Geological Magazine, 145(1), 37–54. doi: 10.1017/S0016756807003986.

Aldanmaz E. 2002. Mantle source characteristics of alkali basalts and basanites in an extensional intracontinental plate setting, western Anatolia, Turkey: implications for multi-stage melting. International Geology Review, 44(5), 440–457. doi: 10.2747/0020-6814.44.5.440.

Allegre CJ, Minster JF. 1978. Quantitative method of trace element behavior in magmatic processes. Earth and Planetary Science Letters, 38, 1–25. doi: 10.1016/0012-821X(78)90123-1.

Babechuk MG, Widdowson M, Murphy M, Kamber BS. 2014. A combined Y/Ho, high field strength element (HFSE) and Nd isotope perspective on basalt weathering, Deccan Traps, India. Chemical Geology.

Basak A, Goswami B, Singha A, Das S, Bhattacharyya C. 2019. Magmatic epidote in the Grenvillian granitoids of North Purulia Shear Zone, Chhotanagpur Gneissic Complex, India and its significance; Current Science, (00113891), 117(2).

Basak A, Goswami B. 2020. The physico-chemical conditions of crystallization of the Grenvillian arfvedsonite granite of Dimra Pahar, Hazaribagh, India: constraints on possible source regions. Mineralogy and Petrology, 114, 329–356. doi: 10.1007/s00710-020-00708-w.

Bhattacharya DK, Mukherjee D, Barla VC. 2010. Komatiite within Chhotanagpur Gneissic Complex at Semra, Palamau district, Jharkhand: petrological and geochemical fingerprints. Journal of the Geological Society of India, 76(6), 589–606. doi: 10.1007/s12594-010-0120-y.

Bhattacharyya PK, Mukherjee S. 1987. Granulites in and around the Bengal anorthosite, eastern India: genesis of coronal garnet and evolution of the granulite–anorthosite complex. Geological Magazine, 124, 21–32. doi: 10.1017/S0016756800015752.

Bhowmik SK, Wilde SA, Bhandari A, Pal T, Pant NC. 2012. Growth of the Greater Indian Landmass and its assembly in Rodinia: geochronological evidence from the Central Indian Tectonic Zone. Gondwana Research, 22, 54–72. doi: 10.1016/j.gr.2011.09.008.

Blundy JD, Holland TJB. 1990. Calcic amphibole equilibria and a new amphibole-plagioclase geothermometer. Contributions to Mineralogy and Petrology, 104(2), 208–224. doi: 10.1007/BF00306444.

Brandl PA, Genske FS, Beier C, Haase KM, Sprung P, Krumm SH. 2015. Magmatic evidence for carbonate metasomatism in the lithospheric mantle underneath the Ohře (Eger) Rift. Journal of Petrology, 56(9), 1743–1774. doi: 10.1093/petrology/egv052.

Bright RM, Amato JM, Denyszyn SW, Ernst RE. 2014. U-Pb geochronology of 1. 1 Ga diabase in the southwestern United States:Testing models for the origin of a post-Grenville large igneous province. Lithosphere, 6(3), 135–156.

Chatterjee N, Crowley JL, Ghose NC. 2008. Geochronology of the 1.55 Ga Bengal anorthosite and Grenvillian metamorphism in the Chotanagpur gneissic complex, eastern India. Precambrian Research, 161, 303–316.

Chen G, Sun D, Hui'an Yin. 1988. Genetic mineralogy and prospecting mineralogy. Chongqing Publishing House.

Choudhary BR, Ernst RE, Xu YG, Evans DA, de Kock MO, Meert JG, Ruiz AS, Lima GA. 2019. Geochemical characterization of a reconstructed 1110 Ma large igneous province. Precambrian Research, 332, 105382. doi: 10.1016/j.precamres.2019.105382.

Claiborne LL, Miller CF, Walker BA, Wooden JL, Mazdab FK, Bea F. 2006. Tracking magmatic processes through Zr/Hf ratios in rocks and Hf and Ti zoning in zircons: an example from the Spirit Mountain batholith, Nevada. Mineralogical Magazine, 70(5), 517–543. doi: 10.1180/0026461067050348.

Condie KC. 1997. Sources of Proterozoic mafic dyke swarms: constraints from ThTa and LaYb ratios. Precambrian Research, 81(1-

2), 3–14. doi: 10.1016/S0301-9268(96)00020-4.
Connolly JAD. 2005. Computation of phase equilibria by linear programming: A tool for geodynamic modelling and its application to subduction zone decarbonation. Earth and Planetary Science Letters, 236, 524–541. doi: 10.1016/j.epsl.2005.04.033.
Correa-Gomes LC, Oliveira EP. 2000. Radiating 1. 0 Ga mafic dyke swarms of eastern Brazil and western Africa:evidence of post-assembly extension in the Rodinia supercontinent?. Gondwana Research, 3(3), 325–332.
Cox K, G Bell, JD Pankhurst, RJ. 1979. The interpretation of igneous rocks. London: Allen and Unwin.
Currie KL, Williams PR. 1993. An Archeancalc-alkaline lamprophyre suite, northeasternYilgarn Block, western Australia. Lithos, 31(1-2), 33–50. doi: 10.1016/0024-4937(93)90031-7.
Das S, Goswami B, Basak A, Bhattacharyya C. 2020. A Grenvillian magmatic almandine garnet-bearing ferroan granite intrusion in the Chhotanagpur Gneissic complex, Eastern India; Petrology, petrochemistry, petrogenesis and geodynamic implications. Lithos, 376, 105749.
Dasgupta R, Hirschmann MM, Smith ND. 2007. Partial melting experiments of peridotite+ CO_2 at 3 GPa and genesis of alkalic ocean island basalts. Journal of Petrology, 48(11), 2093–2124. doi: 10.1093/petrology/egm053.
Deer WA, Howie RA, Zussman J. 1992. An introduction to the rock-forming minerals. Longman, London, 696.
Dey A, Karmakar S, Mukherjee S, Sanyal S, Dutta U, Sengupta P. 2019. High pressure metamorphism of mafic granulites from the Chotanagpur Granite Gneiss Complex, India: Evidence for collisional tectonics during assembly of Rodinia. Journal of Geodynamics, 129, 24–43. doi: 10.1016/j.jog.2019.03.005.
Elburg MA, Van Bergen M, Hoogewerff J, Foden J, Vroon P, Zulkarnain I, Nasution A. 2002. Geochemical trends across an arc-continent collision zone: magma sources and slab-wedge transfer processes below the Pantar Strait volcanoes, Indonesia. Geochimica et Cosmochimica Acta, 66(15), 2771–2789. doi: 10.1016/S0016-7037(02)00868-2.
Elling R, Stein S, Stein CA, Gefeke K. 2022. Three Major Failed Rifts in Central North America: Similarities and Differences. GSA Today, 32(6), 4–11. doi: 10.1130/GSATG518A.1.
Erlank AJ, Duncan AR, Marsh JS, Sweeney RJ, Hawkesworth CJ, Milner SC, Miller RM, Rogers NW. 1988. A laterally extensive geochemical discontinuity in the subcontinental Gondwana lithosphere. Proceedings of the V Conference on Geochemical Evolution of the Continental Crust, Brazil, 1–10.
Ernst RE, Buchan KL. 2001. The use of mafic dyke swarms in identifying and locating mantle plumes. In: Ernst RE, Buchan KL (eds) Mantle plumes: their identification through time. Special Paper of the Geological Society of America, 352, 247–265.
Ernst RE. 2014. Large igneous provinces. Cambridge University Press, 653.
Evans DAD. 2013. Reconstructing pre-Pangean supercontinents. Bulletin of the Geological Society of America, 125, 1735–1751. doi: 10.1130/B30950.1.
Evins PM, Smithies RH, Howard HM, Kirkland CL, Wingate MT, Bodorkos S. 2010. Devil in the detail: The 1150–1000 Ma magmatic and structural evolution of the Ngaanyatjarra Rift, west Musgrave Province, Central Australia. Precambrian Research, 183(3), 572–588. doi: 10.1016/j.precamres.2010.02.011.
Ferry JT, Spear FS. 1978. Experimental calibration of the partitioning of Fe and Mg between biotite and garnet. Contributions to Mineralogy and Petrology, 66(2), 113–117. doi: 10.1007/BF00372150.
Floyd PA, Kelling G, Gökçen SL, Gökçen N. 1991. Geochemistry and tectonic environment of basaltic rocks from the Misis ophiolitic mélange, south Turkey. Chemical Geology, 89(3-4), 263–280. doi: 10.1016/0009-2541(91)90020-R.
Fuhrman ML, Lindsley DH. 1988 Ternary-Feldspar Modeling and Thermometry. American Mineralogist, 73, 201–15.
Furman T, Graham D. 1999. Erosion of lithospheric mantle beneath the East African Rift system: geochemical evidence from the Kivu volcanic province. In:Developments in Geotectonics, Elsevier, 24,237–262.
Gale A, Dalton CA, Langmuir CH, Su Y, Schilling JG. 2013. The mean composition of ocean ridge basalts. Geochemistry, Geophysics, Geosystems, 14(3), 489–518.
Gasparik T. 1984. Experimental study of subsolidus phase relations and mixing properties of pyroxene in the system CaO-Al_2O_3-SiO_2. Geochimica et Cosmochimica Acta, 48, 2537–45. doi: 10.1016/0016-7037(84)90304-1.
Gasparik T. 1985. Experimental study of subsolidus phase relations and mixing properties of pyroxene and plagioclase in the system Na_2O-CaO-Al_2O_3-SiO_2. Contributions to Mineralogy and Petrology, 89, 346–57. doi: 10.1007/BF00381556.
Ghatak A, Basu AR, Wakabayashi J. 2012. Elemental mobility in subduction metamorphism: Insight from metamorphic rocks of the Franciscan Complex and the Feather River ultramafic belt, California. International Geology Review, 54(6), 654–685. doi: 10.1080/00206814.2011.567087.
Ghose NC, Chatterjee N. 2008. Petrology, tectonic setting and source of dykes and related magmatic bodies in Chotanagpur gneissic complex, eastern India. In: Srivastava RK, Sivaji C, ChalapathiRao NV (Eds.), Indian Dyke: Geochemistry, Geophysics and Geochronology. Narosa Publishing House Private Limited, New Delhi, 471–493.
Ghose NC, Mukherjee D, Chatterjee N. 2005. Plume generated Mesoproterozoic mafic-ultramafic magmatism in the Chotanagpur mobile belt of Eastern Indian shield margin. Journal of the Geological Society of India, 66, 725–740.
Ghose NC. 1983. Geology, tectonics and evolution of the Chotanagpur granite gneiss complex, Eastern India. In: Sinha Roy, S. (Ed.); Recent Researches in Geology, 10 211-247.
Giuseppe P Di, Agostini S, Manetti P, Savaşçın MY, Conticelli S. 2018. Sub-lithospheric origin of Na-alkaline and calc-alkaline magmas in a post-collisional tectonic regime: Sr-Nd-Pb isotopes in recent monogenetic volcanism of Cappadocia, Central Turkey. Lithos, 316, 304–322.
Goswami B, Bhattacharyya C. 2008. Metamorphism of nepheline syenite gneisses from chhotanagpur granite gneiss complex, Northeastern Puruliya district, Eastern India. Journal Geological Society of India. 71(2), 209–213.
Goswami B, Bhattacharyya C. 2010. Tectonothermal evolution of Chhotanagpur granite gneiss complex from northeastern part of Puruliya district, West Bengal, eastern Indian. Indian Journal of Geosciences, 80(1–4), 41–54.
Goswami B, Bhattacharyya C. 2014. Petrogenesis of shoshonitic granitoids, eastern India: implications for the late Grenvillian post-collisional magmatism. Geoscience Frontier, 5, 21–43.
Goswami B, Roy P, Basak A, Das S, Bhattacharyya C. 2018. Physicochemical conditions of four calc-alkaline granitoid plutons of Chhotanagpur Gneissic Complex, Eastern India: tectonic implications. Journal of Earth System Sciences, 127, 1–33. doi: 10.1007/s12040-017-0916-x.
Hammarstrom JM, Zen EA. 1986 Aluminum-in-hornblende: An empirical igneous geobarometer. American Mineralogist, 71(11–12), 1297–1313
Han S, Li M, Zhang Q, Song L. 2020. An Automated Method to Generate and Evaluate Geochemical Tectonic Discrimination Diagrams Based on Topological Theory. Minerals, 10(1), 62. doi: 10.3390/min10010062.

Hanson RE, Crowley JL, Bowring SA, Ramezani J, Gose WA, Dalziel IW, Pancake JA, Seidel EK, Blenkinsop TG, Mukwakwami J. 2004. Coeval large-scale magmatism in the Kalahari and Laurentian cratons during Rodinia assembly. Science, 304(5674), 1126–1129. doi: 10.1126/science.1096329.

Harlov DE. 2012. The potential role of fluids during regional granulite-facies dehydration in the lower crust. Geoscience Frontier, 3(6), 813–827. doi: 10.1016/j.gsf.2012.03.007.

Hart WK, Wolde GC, Walter RC, Mertzman SA. 1989. Basaltic volcanism in Ethiopia: constraints on continental rifting and mantle interactions. Journal of geophysical research, 94, 7731–7748. doi: 10.1029/JB094iB06p07731.

Hawkesworth CJ, Turner SP, McDermott F, Peate DW, Van Calsteren P. 1997. U-Th isotopes in arc magmas: Implications for element transfer from the subducted crust. Science, 276(5312), 551–555. doi: 10.1126/science.276.5312.551.

Hill IG, Worden RH, Meighan IG. 2000. Geochemical evolution of a palaeolaterite: The Inter basaltic Formation, Northern Ireland. Chemical Geology, 166, 65–84. doi: 10.1016/S0009-2541(99)00179-5.

Hirose K, Kushiro I. 1993. Partial melting of dry peridotites at high pressures: determination of compositions of melts segregated from peridotite using aggregates of diamond. Earth and Planetary Science Letters, 114(4), 477–489. doi: 10.1016/0012-821X(93)90077-M.

Hoisch TD. 1990. Empirical calibration of six geobarometers for the mineral assemblage quartz + muscovite + biotite + plagioclase + garnet. Contributions to Mineralogy and Petrology, 104(2), 225–234. doi: 10.1007/BF00306445.

Holland TJB, Blundy J. 1994. Non-ideal interactions in calcic amphiboles and their bearing on amphibole-plagioclase thermometry. Contributions to Mineralogy and Petrology, 116(4), 433–447. doi: 10.1007/BF00310910.

Holland TJB, Powell R. 1996. Thermodynamics of order-disorder in minerals: II. Symmetric formalism applied to solid solutions. American Mineralogist, 81(11–12), 1425–1437.

Holland TJB, Powell R. 2011. An improved and extended internally consistent thermodynamic dataset for phases of petrological interest, involving a new equation of state for solids. Journal of metamorphic Geology, 29(3), 333–383. doi: 10.1111/j.1525-1314.2010.00923.x.

Holland TJB, Powell R. 1998. An internally consistent thermodynamic data set for phases of petrological interest. Journal of Metamorphic Geology, 16, 309–43.

Hollister LS, Grissom GC, Peters EK, Stowell HH, Sisson VB. 1987. Confirmation of the empirical correlation of Al in hornblende with pressure of solidification of calc-alkaline plutons. American Mineralogist, l 72 (3–4), 231–239

Holmes A. 1955. Dating the Precambrian of Peninsular India and Ceylon. Proceedings of the Geologists Association of Canada, 7, 81–106.

Hoskin PW, Schaltegger U. 2003. The composition of zircon and igneous and metamorphic petrogenesis. Reviews in mineralogy and geochemistry, 53(1), 27–62. doi: 10.2113/0530027.

Howard HM, Smithies RH, Kirkland CL, Evins PM, Wingate MTD. 2009. Age and geochemistry of the Alcurra Suite in the west Musgrave Province and implications for orthomagmatic Ni–Cu–PGE mineralization during the Giles Event. Geological Survey of Western Australia, Record, 16,16.

Hu Y, Zhao X, Peng P, Yang F, D'Agrella-Filho MS, Chen W, Xu M. 2022. Paleomagnetic Constraints From 925 Ma Mafic Dykes in North China and Brazil: Implications for the Paleogeography of Rodinia. Journal of Geophysical Research:Solid Earth, 127(9), 2022JB025079. doi: 10.1029/2022JB025079.

Irvine TNJ, Baragar WRAF. 1971. A guide to the chemical classification of the common volcanic rocks. Canadian Journal of Earth Sciences, 8(5), 523–548. doi: 10.1139/e71-055.

Jin SQ. 1991. Compositional characteristics of calcareous amphibole from metamorphic facies in different regions. Chinese Science Bulletin 36, 851–854 (in Chinese).

Johnson MC, Rutherford MJ. 1989. Experimental calibration of the aluminum-in-hornblende geobarometer with application to Long Valley caldera (California) volcanic rocks. Geology, 17(9), 837–841. https://doi.org/10.1130/0091-7613(1989)017<0837:ECOTAI>2.3.CO;2.

Jourdan F, Bertrand H, Féraud G, Le Gall B, Watkeys MK. 2009. Lithospheric mantle evolution monitored by overlapping large igneous provinces: case study in southern Africa. Lithos, 107, 257–268. doi: 10.1016/j.lithos.2008.10.011.

Karmakar S, Bose S, Sarbadhikari AB, Das K. 2011. Evolution of granulite enclaves and associated gneisses from Purulia, Chhotanagpur Granite Gneiss Complex, India: evidence for 990–940 Ma tectonothermal event(s) at the eastern India cratonic fringe zone. Journal of Asian Earth Sciences, 41, 69–88. doi: 10.1016/j.jseaes.2010.12.006.

Klein EM. 2003. Geochemistry of the Igneous oceanic rocks. The crust, 3, 433.

Kretz R. 1982. Transfer and exchange equilibria in a portion of the pyroxene quadrilateral as deduced from natural and experimental data. Geochimica et Cosmochimica Acta, 46(3), 411–421. doi: 10.1016/0016-7037(82)90232-0.

Krishnan MS. 1961. Tectonics with special reference to India. Proceedings of the Indian Academy of Sciences Section B, 53, 49–72. doi: 10.1007/BF03050924.

Kumar A, Ahmad T. 2007. Geochemistry of the mafic dykes in parts of Chotanagpur gneissic complex: petrogenetic and tectonic implications. Geochemical Journal, 41, 173–186. doi: 10.2343/geochemj.41.173.

Kumar D, Rao NC, Prabhat P, Chatterjee A, Rahaman W. 2022. Petrochemistry and Sr-Nd isotopes of post-collisional Neoproterozoic (ca. 950 Ma) amphibolite dykes of continental flood basalt affinity from the Simdega area: Implications for the geodynamic evolution of the Chhotanagpur Gneissic Complex, Eastern India. Lithos. 1;428: 106810.

La Flèche MR, Camire G, Jenner GA. 1998. Geochemistry of post-Acadian, Carboniferous continental intraplate basalts from the Maritimes Basin, Magdalen islands, Quebec, Canada. Chemical Geology, 148, 115–136. doi: 10.1016/S0009-2541(98)00002-3.

Langmuir CH, Klein EM, Plank T. 1992. Petrological systematics of mid-ocean ridge basalts: Constraints on melt generation beneath ocean ridges. Mantle flow and melt generation at mid-ocean ridges. Geophysical Monograph- American Geophysical Union, 71, 183–280.

Le Cheminant AN, Heaman LM. 1989. Mackenzie igneous events, Canada: Middle Proterozoic hotspot magmatism associated with ocean opening. Earth and Planetary Science Letters, 96, 38–48. doi: 10.1016/0012-821X(89)90122-2.

Li ZX, Bogdanova S, Collins AS, Davidson A, De Waele B, Ernst RE, Fitzsimons ICW, Fuck RA, Gladkochub DP, Jacobs J, Karlstrom KE. 2008. Assembly, configuration, and break-up history of Rodinia: a synthesis. Precambrian research, 160(1–2), 179–210. doi: 10.1016/j.precamres.2007.04.021.

Luttinen AV. 2018. Bilateral geochemical asymmetry in the Karoo large igneous province. Scientific reports, 8(1), 5223. doi: 10.1038/s41598-018-23661-3.

Mahadevan TM. 2002. Geology of Bihar and Jharkhand. Geological Society of India Bangalore, 563.

Maji AK, Goon S, Bhattacharya A, Mishra B, Mahato S, Bernhardt HJ. 2008. Proterozoic polyphase metamorphism in the Chhotanagpur Gneissic Complex (India), and implication for trans-continental Gondwanaland correlation. Precambrian Research, 162(3), 385–402.

Martinez-serrano R, Schaaf P, Solís-Pichardo G, Hernández-Bernal MD, Hernández-Treviño T, Morales-Contreras J, Macías JL. 2004. Sr, Nd and Pb isotope and geochemical data from the Quaternary Nevado de Toluca volcano, a source of recent adakiticmagmatism, and the Tenango Volcanic Field, Mexico. Journal of Volcanology and Geothermal Research, 138, 77–110. doi: 10.1016/j.jvolgeores.2004.06.007.

Maruyama S, Liou JG, Terabayashi M. 1996. Blueschists and eclogites of the world and their exhumation. International Geology Review. 38(6), 485–594.

Mason B, Moore CB. 1982. Principles of Geochemistry. Wiley, New York.

Mamouda Aliou, Ganno Sylvestre, Bertin Guy Tchoupe Takam, Steven Arnold Mbita Motto, Fossi Hermann Donald, Nzenti Jean Paul, Ondoa Joseph Mvondo. 2022. Origin and intraplate tectonic setting of mafic magmatic enclaves from the Ngaoundal area, Adamawa-Cameroon: Insights from petrography and geochemistry. China Geology, 5(4), 579–594. doi: 10.31035/cg2022041.

Mazumdar SK. 1988. Crustal evolution of Chhotanagpur gneissic complex and the mica belt of Bihar. In: Mukhopadhyay, D. (Ed.), Precambrian of the Eastern Indian Shield. Memoirs, Geological Society of India, 8, 49–83.

McDonough WF, Sun SS. 1995. The composition of the earth. Chemical Geology, 120, 223–53. doi: 10.1016/0009-2541(94)00140-4.

Mertanen S, Pesonen LJ, Huhma H. 1996. Palaeomagnetism and Sm-Nd ages of the Neoproterozoic diabase dykes in Laanila and Kautokeino, northern Fennoscandia. Geological Society, London, Special Publications, 112(1), 331–358.

Miyashiro A. 1975. Volcanic rock series and tectonic setting. Annual Review of Earth and Planetary Sciences, 3(1), 251–269. doi: 10.1146/annurev.ea.03.050175.001343.

Mukherjee S, Dey A, Ibanez-Mejia M, Sanyal S, Sengupta P. 2018. Geochemistry, U–Pb geochronology and Lu–Hf isotope systematics of a suite of ferroan (A-type) granitoids from the CGGC: Evidence for Mesoproterozoic crustal extension in the East Indian shield. Precambrian Research, 305, 40–63. doi: 10.1016/j.precamres.2017.11.018.

Mukherjee S, Dey A, Sanyal S, Ibanez‐Mejia, M, Dutta U, Sengupta P. 2017. Petrology and U–Pb geochronology of zircon in a suite of charnockitic gneisses from parts of the Chotanagpur Granite Gneiss Complex (CGGC): Evidence for the reworking of a Mesoproterozoic basement during the formation of the Rodinia supercontinent. Geological Society, London, Special Publication, l457, 457–456.

Naganjaneyulu K, Santosh M. 2010. The Central India Tectonic Zone: a geophysical perspective on continental amalgamation along a Mesoproterozoic suture. Gondwana Research, 18(4), 547–564. doi: 10.1016/j.gr.2010.02.017.

Otten MT. 1984. The origin of brown hornblende in the Artfjället gabbro and dolerites. Contributions to Mineralogy and Petrology, 86(2), 189–199. doi: 10.1007/BF00381846.

Pearce JA, Ernst RE, Peate DW, Rogers C. 2021. LIP printing: Use of immobile element proxies to characterize Large Igneous Provinces in the geologic record. Lithos, 392–393, 106068.

Pearce JA. 1996. A user's guide to basalt discrimination diagrams. Trace element geochemistry of volcanic rocks: applications for massive sulphide exploration. Geological Association of Canada, Short Course Notes, 12(79), 113.

Pearce JA. 2008. Geochemical fingerprinting of oceanic basalts with applications to ophiolite classification and the search for Archean oceanic crust. Lithos, 100, 14–48. doi: 10.1016/j.lithos.2007.06.016.

Philpotts A, Ague J. 2009. Principles of igneous and metamorphic petrology. Cambridge University Press.

Polat A, Hofmann AW, Rosing MT. 2002. Boninite-like volcanic rocks in the 3.7–3.8 GaIsua greenstone belt, West Greenland: geochemical evidence for intra-oceanic subduction zone processes in the early Earth. Chemical Geology, 184(3–4), 231-254.

Polat A, Hofmann AW. 2003. Alteration and geochemical patterns in the 3.7–3.8 Ga Isua greenstone belt, West Greenland. Precambrian Research, 126(3–4), 197–218.

Pradhan VR, Meert JG, Pandit MK, Kamenov G, Mondal ME A. 2012. Paleomagnetic and geochronological studies of the mafic dyke swarms of Bundelkhand craton, central India. Precambrian Research, 305, 40–63.

Radhakrishna BP. 1989. Suspect tectono-stratigraphic terrane elements in the Indian subcontinent. The Journal of the Geological Society of India, 34, 1–24.

Ray Barman T, Bishui PK, Mukhopadhyay K, Ray JN. 1994. Rb-Sr geochronology of the high grade rocks from Purulia, West Bengal and Jamua-Dumka sector, Bihar. Indian Minerals, 48, 45–60.

Rekha S, Upadhyay D, Bhattacharya A, Kooijman E, Goon S, Mahato S, Pant NC. 2011. Lithostructural and chronological constraints for tectonic restoration of Proterozoic accretion in the Eastern Indian Precambrian shield. Precambrian Research, 187, 313–33. doi: 10.1016/j.precamres.2011.03.015.

Ridolfi F, Renzulli A, Puerini M. 2010. Stability and chemical equilibrium of amphibole in calc-alkaline magmas: An overview, new thermobarometric formulations and application to subduction-related volcanoes. Contributions to Mineralogy and Petrology, 160(1), 45–66. doi: 10.1007/s00410-009-0465-7.

Rollinson HR. 1993. Using Geochemical Data: Evaluation, Presentation, Interpretation. Wiley New York.

Roy AK. 1977. Structural and metamorphic evolution of the Bengal anorthosites and associated rocks. Journal of the Geological Society of India, 203–223.

Roy P, Goswami B, Dutta S, Bhattacharyya C. 2020. Petrogenesis of the post-collisional porphyritic granitoids from Jhalida, Chhotanagpur Gneissic Complex, eastern India. Geological Magazine, 158(4), 598–634.

Saccani E. 2015. A new method of discriminating different types of post-Archean ophiolitic basalts and their tectonic significance using Th-Nb and Ce-Dy-Yb systematics. Geoscience Frontiers, 6(4), 481–501. doi: 10.1016/j.gsf.2014.03.006.

Sanyal S, Sengupta P. 2012. Metamorphic evolution of the Chotanagpur Granite Gneiss Complex of the East Indian Shield: current status. In: Mazumder, R. , Saha, D. (Eds.), Palaeoproterozoic of India. Geological Society, London, Special Publication, 365, 117–145.

Schmidt M. 1992. Amphibole composition in tonalite as a function of pressure: an experimental calibration of the Al-in-hornblende barometer. Contributions to Mineralogy and Petrology, 110(2), 304–310.

Schweitzer J, Kröner A. 1985. Geochemistry and petrogenesis of early Proterozoic intracratonic volcanic rocks of the Ventersdorp Supergroup, South Africa. Chemical Geology, 51(3–4), 265–288. doi: 10.1016/0009-2541(85)90137-8.

Sen SK, Bhattacharya A. 1986. Fluid induced metamorphic changes in the Bengal anorthosite around Saltora, West Bengal, India. Indian Journal of Earth Sciences, 13, 45–64.

Sen SK, Bhattacharya A. 1993. Post peak pressure-temperature-fluid history of the granulites around Saltora, West Bengal. Proceedings of the National Academy of Sciences, India, 63(A)(1), 280–306.

Sequeira N, Mahato S, Rahl JM, Sarkar S, Bhattacharya A, Nance D. 2020. The Anatomy and Origin of a Syn convergent Grenvillian-Age Metamorphic Core Complex, Chottanagpur Gneiss Complex, Eastern India. Lithosphere, 2020(1).

Sharma RS 2009. Cratons and Fold belts of India. Springer, 304.

Sharma RS, Sills JD, Joshi M. 1987. Mineralogy and metamorphic history of norite dykes within granulite facies gneisses from Sand Mata, Rajasthan, NW India. Mineralogical Magazine, 51(360),

207–215. doi: 10.1180/minmag.1987.051.360.03.

Shervais JW. 1982. Ti–V plots and petrogenesis of modern and ophiolitic lavas. Earth and Planetary Science Letters, 59, 101–118. doi: 10.1016/0012-821X(82)90120-0.

Singh Y, Krishna V. 2009. Rb-Sr geochronology and petrogenesis of granitoids from the Chhotanagpur granite gneiss complex of Raikera-Kunkuri region, Central India. Journal of the Geological Society of India, 74(2), 200–208. doi: 10.1007/s12594-009-0122-9.

Singh Y, Rai SD. 1992. Yttrium-europium-erbium geochemistry of granitic soils of Kunkuri area, Raigarh district, M. P. , India. Journal of the Geological Society of India, 40, 347–358.

Smith EI, Sanchez A, Walker JD, Wang K. 1999. Geochemistry of mafic magmas in the Hurricane Volcanic field, Utah: implications for small-and large-scale chemical variability of the lithospheric mantle. The Journal of Geology, 107(4), 433–448. doi: 10.1086/314355.

Srivastava RK, Sinha AK, Kumar S. 2012. Geochemical characteristics of Mesoproterozoic metabasite dykes from the Chhotanagpur Gneissic Terrain, eastern India: implications for their emplacement in a plate margin tectonic environment. Journal of Earth System Sciences, 121, 509–523. doi: 10.1007/s12040-012-0172-z.

Stein S, Stein CA, Elling R, Kley J, Keller GR, Wysession M, Rooney T, Frederiksen A, Moucha R. 2018. Insights from North America's failed Midcontinent Rift into the evolution of continental rifts and passive continental margins. Tectonophysics, 744, 403–421. doi: 10.1016/j.tecto.2018.07.021.

Su X, Peng P, Foley S, Teixeira W, Zhai MG. 2021. Initiation of continental breakup documented in evolution of the magma plumbing system of the ca. 925 Ma Dashigou large igneous province, North China. Lithos, 384, 105984.

Sun SS, McDonough WF. 1989. Chemical and isotopic systematics of oceanic basalts: implications for mantle composition and processes. Special Publications. In: Saunders, A. D.

Unrug R. 1996. The assembly of Gondwanaland. Episodes, 19, 11–20. doi: 10.18814/epiiugs/1996/v19i1.2/004.

Wang L, Kusky TM, Polat A, Wang S, Jiang X, Zong K, Wang J, Deng H, Fu J. 2014. Partial melting of deeply subducted eclogite from the Sulu orogen in China. Nature communications, 5(1), 5604. doi: 10.1038/ncomms6604.

Wang P, Ren Y, Shan X, Sun S, Wan C, Bian W 2002 The Cretaceous volcanic succession around the Songliao Basin, NE China: relationship between volcanism and sedimentation. Geological Journal, 37(2), 97–115.

Weaver BL, Tarney J. 1981. Chemical changes during dyke metamorphism in high-grade basement terrains. Nature, 289(5793), 47–49. doi: 10.1038/289047a0.

Wells PRA. 1977. Pyroxene thermometry in simple and complex system. Contribution to Mineralogy and Petrology, 62, 129–139. doi: 10.1007/BF00372872.

Whitney DL, Evans BW. 2010. Abbreviations for names of rock-forming minerals. American mineralogist, 95(1), 185–187. doi: 10.2138/am.2010.3371.

Wingate MT, Pirajno F, Morris PA. 2004. Warakurna large igneous province: A new Mesoproterozoic large igneous province in west-central Australia. Geology, 32(2), 105–108. doi: 10.1130/G20171.1.

Xie Hong-zhe, Zhu Xiang-kun, Wang Xun, He Yuan, Shen Wei-bing. 2023. Petrological and geochemical characteristics of mafic rocks from the Neoproterozoic Sugetbrak Formation in the northwestern Tarim Block, China. China Geology, 6(1), 85–99. doi: 10.31035/cg2021067.

Xu YG. 2001. Thermo-tectonic destruction of the Archaean lithospheric keel beneath the Sino-Korean Craton in China: Evidence, timing and mechanism. Physics and Chemistry of the Earth, Part A: Solid Earth and Geodesy, 26(9–10), 747–757.

Xue JZ, Bai XR, Chen W. 1986. Genetic mineralogy. China University of Geosciences Press, Wuhan (in Chinese).

Zeng G, Chen LH, Xu XS, Jiang SY, Hofmann AW. 2010. Carbonated mantle sources for Cenozoic intra-plate alkaline basalts in Shandong, North China. Chemical Geology, 273(1–2), 35–45. doi: 10.1016/j.chemgeo.2010.02.009.

Zhang X, Su Y, Zheng J, Liu P, Griffin WL, Ping X, Wang J, Zhou L. 2021. Metamorphic history and Neoarchean–Paleoproterozoic crustal growth of the central Trans-North China Orogen: Evidence from granulite-to amphibolite-facies rocks of the Hengshan complex. Gondwana Research, 93, 162–183. doi: 10.1016/j.gr.2021.02.004.